UNIVERSITY OF CALGARY

Exploring Stream Accretion in High Mass X-ray Binaries

by

Mathew Kostka

A THESIS

SUBMITTED TO THE FACULTY OF GRADUATE STUDIES

IN PARTIAL FULFILMENT OF THE REQUIREMENTS FOR THE

DEGREE OF MASTER OF SCIENCE

DEPARTMENT OF PHYSICS AND ASTRONOMY

CALGARY, ALBERTA

SEPTEMBER 2009

UNIVERSITY OF CALGARY

FACULTY OF GRADUATE STUDIES

The undersigned certify that they have read, and recommend to the Faculty of Graduate Studies for acceptance, a thesis entitled "Exploring Stream Accretion in High Mass X-ray Binaries" submitted by Mathew Kostka in partial fulfilment of the requirements of the degree of Master of Science.

Supervisor, Denis Leahy, Department of Physics and Astronomy

Jo-Anne Brown, Department of Physics and Astronomy

David Knudsen, Department of Physics and Astronomy

External Examiner, Tom Ziegler, Chemistry Department

Aug 27, 2009

Date

Abstract

This work focuses on the method of accretion in supergiant X-ray binary systems. Analysis of twelve years of observations from the Rossi X-ray Timing Explorer All-Sky Monitor folded at the orbital period is carried out for the following systems: 4U 1907+09, GX 301-2, OAO 1657-415 and 2S 0114+650. Each orbital X-ray light curve is compared to the expected light curve of a system with the mechanism of accretion being a stream originating at the surface of the companion star along with strong stellar winds. Orbital parameters of each system are taken as inputs for the wind and stream accretion model and statistical analysis is done to constrain the properties of the stellar wind and gas stream. We find that the systems 4U 1907+09 and GX 301-2 likely contain a dynamic gas stream that significantly contributes to the production of X-ray radiation. Further analysis is required to accurately determine the accretion mechanism in OAO 1657-415; preliminary results point to the possibility of stream accretion. The binary system 2S 0114+650 appears to be undergoing accretion via stellar wind capture.

Table of Contents

Abstract ii
Table of Contents iii
List of Tables v
List of Figures and Illustrations vi
List of Symbols, Abbreviations and Nomenclature x

CHAPTER ONE: INTRODUCTION 1

CHAPTER TWO: BACKGROUND 4
2.1 X-ray Binary Star Systems 4
2.1.1 Low Mass X-ray Binaries 4
2.1.2 Be-Transient Binaries 5
2.1.3 High Mass X-ray Binaries 6
2.2 Pulsars 8
2.3 Supergiant Stars 13
2.4 Geometry of Binary System 16

CHAPTER THREE: ACCRETION 22
3.1 Roche Geometry 25
3.2 Disk Accretion 28
3.3 Wind Accretion 29
3.3.1 Radial Wind Velocity 36
3.4 Stream Accretion 37
3.4.1 Dynamic Accretion Stream 39
3.4.1.1 Current Methodology 48

CHAPTER FOUR: OBSERVATIONS 53
4.1 Instrumentation 53
4.1.1 Rossi X-ray Timing Explorer All-Sky Monitor 55
4.2 Data Analysis 58
4.2.1 Epoch Folding 59

CHAPTER FIVE: RESULTS AND ANALYSIS 62
5.1 4U 1907+09 64
5.1.1 Column Density Analysis 70
5.2 GX 301-2 75
5.3 OAO 1657-415 78
5.4 2S 0114+650 81

CHAPTER SIX: DISCUSSION 84
6.1 4U 1907+09 84
6.2 GX 301-2 87
6.3 OAO 1657-415 88
6.4 2S 0114+650 90

6.5 Overview....91
6.6 Future Work....91

BIBLIOGRAPHY....93

List of Tables

Table 2.1 Selected HMXB systems 7

Table 2.2 Orbital Elements of Selected HMXBs 21

Table 5.1 Mean Roche lobe radii for 4U 1907+09 66

Table 5.2 Best fit values for 4U 1907+09 with eccentricity 0.25 66

Table 5.3 Best fit values for 4U 1907+09 with eccentricity 0.28 67

Table 5.4 Best fit values for 4U 1907+09 with eccentricity 0.31 67

Table 5.5 Best fit values for 4U 1907+09 with radius 16.45 $R_{\odot}$ 68

Table 5.6 Best fit values for GX 301-2 76

Table 5.7 Best fit values for OAO 1657-415 79

Table 5.8 Mean Roche lobe radii for 2S 0114+650 81

Table 5.9 Best fit parameters for 2S 0114+650 82

List of Figures and Illustrations

Figure 2-1 Galactic distribution of selected HMXBs plotted in Galactic coordinates. Note that each system is located within a few degrees of the midline of the Galactic disk. 8

Figure 2-2 Schematic representation of Pulsar geometry. The misalignment of the magnetic or beaming axis from the rotational axis causes observed pulsations (Image from National Radio Astronomy Observatory; www.nrao.edu). 9

Figure 2-3 Mass vs radius diagram for a neutron star. The solid lines indicate equations of state for normal matter and dashed lines represent those of quark matter. Points that fall on a curve represent possible mass and radius values for the neutron star for the given equation of state. The forbidden regions are as well indicated (Lattimer et al. 2004). 10

Figure 2-4 H-R diagram showing luminosity versus spectral class and effective temperature (Image from UCSD Center for Astrophysics & Space Science; cass.ucsd.edu). 14

Figure 2-5 Schematic diagrams of the orbital system for each studied HMXB. For each system the assumed direction of orbit is counter-clockwise. The labelled values denote the following: A – apastron, P – periastron, N – location of the ascending node, $T_{\frac{\pi}{2}}$ - orbital epoch. 17

Figure 2-6 Sketch of geometry of binary orbit. The system inclination, location of the ascending node, longitude of periastron, as well as the projected and true semimajor axes are plotted, see the text for their definitions. The plane of the sky is perpendicular to the line of sight toward Earth. 19

Figure 2-7 Geometry of an elliptical orbit, ψ denotes the eccentric anomaly and θ indicates the polar angle of the neutron star, C denotes the center of the ellipse (Image from Wikipedia, author: Lasunncty) 19

Figure 3-1 Roche geometry for a binary star system; the vertical axis measures the potential energy of the rotating binary and the horizontal axes are spatial dimensions. Above is a three dimensional representation of the distortion of spacetime caused by the two massive bodies. Below is a contour map of gravitational equipotential lines of the system, the five Lagrange points are labelled: L_1, L_2, L_3, L_4 and L_5 and the bold figure eight at the center denotes the Roche lobes of the system (Image from Wikipedia, author:I). 27

Figure 3-2 Mass transfer in binary system. Left: Roche lobe overflow. Right: Accretion due to strong stellar winds. (From Endo 2001) 29

Figure 3-3 Sketch of stellar wind capture. The dashed arrows denote the direction of motion of the stellar wind. Two equal packets of wind material are forced to collide due to the influence of the neutron star's gravity. The resultant velocity ($\vec{v}_f$) of the new packet of wind material must be less than the escape velocity of the neutron star in order for the material to be captured. 30

Figure 3-4 Trajectory of a single packet of wind material (dashed line). The location of the neutron star is denoted by the black dot, which corresponds with the origin of the system. Note that the angular component of position of the wind packet is zero on the right hand side of the neutron star along its midline. 32

Figure 3-5 Evolution of gas packet in accretion stream. The solid line denotes the radial position and the dashed line shows the angular position. Plot is using best fit parameters for GX 301-2 with radius of 62 $R_{\odot}$ and inclination 60° (see chapter five). 44

Figure 3-6 Trajectories of twenty gas packets spaced equally in time. Plot is using best fit parameters for GX 301-2 with radius of 62 $R_{\odot}$ and inclination 60° (see chapter five). The neutron star is orbiting counter-clockwise for this diagram. 45

Figure 3-7 HMXB system GX 301-2 for companion radius $R_c = 62R_{\odot}$ and inclination 60°, including: accretion stream (solid line with circles), companion star (central circle), and the neutron star (small circle) on its orbit (dotted ellipse). Orbital phase 0.2, 0.4, 0.6 and 0.8, (top-left, top-right, bottom-left and bottom-right respectively). 46

Figure 3-8 Gaussian accretion stream components for Leahy 2008 methodology. The plot includes: accretion stream (solid line with circles), companion star (central circle), the neutron star (small circle) on its orbit (dotted ellipse), ϕ_{orb} denotes the angular position of the neutron star and θ_{cross} denotes the angular position of the crossing point of the accretion stream and the neutron star orbit. 47

Figure 3-9 Schematic representation of the density profile of the accretion stream. The shaded area which is centered on the neutron star denotes the portion of the accretion stream that is captured. 49

Figure 3-10 Orientation of capture area with respect to relative velocity of wind and neutron star. ξ denotes the distance from the neutron star to the accretion stream along the line perpendicular to the relative velocity of the stellar wind and the neutron star. 50

Figure 3-11 Approximation used to consider accretion from the gas stream. 51

Figure 4-1 Schematic diagram of a simplified proportional counter. 54

Figure 4-2 Schematic diagram of a scintillation detector. 55

Figure 4-3 Rossi X-ray Timing Explorer. The relative positioning of each instrument aboard the satellite can be seen from this figure. (From NASA website: heasarc.gsfc.nasa.gov/docs/xte/) 57

Figure 4-4 Upper left panel shows the set up of the RXTE-ASM along with the scanning direction and the axis of rotation. Upper right panel display the field of view for RXTE-ASM. The lower panel is a detailed schematic of one of the three scanning shadow cameras that make up RXTE-ASM (From Levine et al. 1996). 57

Figure 4-5 Orbital X-ray light curve for selected HMXBs created from RXTE-ASM data. 61

Figure 5-1 Radius vs. mass plot for the companion in 4U 1907+09. The Roche lobe limit (solid line with open circles) and eclipse limit (dotted line, from Roberts et al. 2001) are shown. 64

Figure 5-2 Geometry of 4U 1907+09 with e=0.31, R_c=16 $R_\odot$ and inc=65° (left: phase point 0.40, right: phase point 0.95). The central circle denotes the companion star and the accretion stream is represented by the dashed line. The neutron star (small circle) sits on its elliptical orbit (dashed line). 68

Figure 5-3 Model fit to RXTE-ASM light curve for 4U 1907+09 with e=0.31, R_c=16 $R_\odot$ and inc=65° (implies M_c=12.9 $M_\odot$). 69

Figure 5-4 Column density versus RXTE-ASM softness ratio for photon index of 1.3, created using WebPIMMS. 70

Figure 5-5 4U 1907+09 softness ratio. 71

Figure 5-6 Column density as a function of orbital phase for 4U 1907+09. 71

Figure 5-7 Column density model fits to RXTE-ASM derived data for 4U 1907+09. The column density model used the best fit parameters from the accretion luminosity model for 4U 1907+09 as inputs 74

Figure 5-8 Radius vs. Mass plot for GX 301-2 (Leahy 2002). 75

Figure 5-9 Model fit to RXTE-ASM light curve for GX 301-2 with R_c=62 $R_\odot$ and inc=60°(implies M_c=53.3 $M_\odot$). 77

Figure 5-10 Mass vs. radius of the companion star in OAO 1657-415. From Chakrabarty 1993. 78

Figure 5-11 Geometry of OAO 1657-415 with Rc=27 $R_{\odot}$ and inc=70° (left: apastron, right: periastron). The central circle denotes the companion star and the accretion stream is represented by the dashed line. The neutron star (small circle) sits on its elliptical orbit (dashed line). 79

Figure 5-12 Model fit to RXTE-ASM light curve for OAO 1657-415 with R_c=27 $R_{\odot}$ and inc=70° (implies M_c=16.6 $M_{\odot}$). 80

Figure 5-13 Model fit to RXTE-ASM light curve for 2S 0114+650 with R_c=38 $R_{\odot}$ and inc=65°........ 83

Figure 6-1 The HMXB 4U 1907+09 at orbital phase 0.2. The line of sight (solid line) points to the neutron star (small circle). The gas stream (dotted line) originates from the companion (central circle). 86

Figure 6-2 OAO 1657-415 Softness ratio 89

List of Symbols, Abbreviations and Nomenclature

Symbol	Definition
HMXB	High Mass X-ray Binary
LMXB	Low Mass X-ray Binary
$R_{\odot}$	Solar Radius
$M_{\odot}$	Solar Mass
$L_{\odot}$	Solar Luminosity
R_n	Neutron Star Radius
M_n, M_x	Neutron Star Mass
R_c	Companion Star Radius
M_c	Companion Star Mass
MHD	Magnetohydrodynamic
RXTE-ASM	Rossi X-ray Timing Explorer All Sky Monitor
RXTE-PCA	Rossi X-ray Timing Explorer Proportional Counter Array
HEXTE	High Energy X-ray Timing Explorer
SSC	Scanning Shadow Camera
PSPC	Position Sensitive Proportional Counter
EDS	Experiment Data System
ρ	Density
B	Magnetic Field Strength
G	Gravitational Constant
P_{orb}	Orbital Period
a	Binary Separation
f_x	X-ray Mass Function
f_c	Optical Mass Function
i, inc	Inclination
v_x	Amplitude of Velocity Variation
e	Eccentricity
ω	Longitude of Periastron
$T_{\pi/2}$	Orbital Epoch
T_{peri}	Date of Periastron Passage
ψ	Eccentric Anomaly
$\dot{m}$	Mass Accretion Rate/Stellar Mass Loss Rate
c	Speed of Light
ΔE	Energy
L_{acc}	Accretion Luminosity
m_e	Electron Mass
m_p	Proton Mass

σ_T	Thompson Scattering Cross Section
F	Force
S	Radiant Energy Flux
L_{edd}	Eddington Luminosity
$\Phi_R(\bar{r})$	Roche Potential
$\bar{\omega}$	Angular velocity
v_{rel}	Relative Velocity
A_{acc}	Accretion Area
R_{acc}	Accretion Radius
v_{rad}	Radial Wind Velocity
v_{az}	Azimuthal Wind Velocity
c_s	Speed of Sound
κ	Bondi-Hoyle Normalization Constant
T_{eff}	Effective Temperature
k_b	Boltzmann Constant
v_∞	Terminal Wind Velocity
ω_{surf}	Angular Velocity of Companion Star
f_1	Companion Rotation Speed Parameter
d_s	Density Enhancement Factor
ξ	Shortest Distance From Neutron Star to Accretion Stream
ξ_{los}	Distance from Neutron Star to Accretion Stream along Line of Sight
r_n	Radial Position of Neutron Star
w_o	Initial Width of Stream
v_{sp}	Spreading Speed of Stream
b	Stream Density Periodicity
q	Mass Ratio
R_{rl}	Mean Roche Lobe Radius
CAK	Castor Abbot Klein
HEASARC	High Energy Astrophysics Science Archive Research Center
N_H	Column Density

Chapter One: Introduction

X-ray binaries are the brightest sources of X-rays in our Galaxy. These systems are composed of a non-compact or *normal* star and a compact star (either a white dwarf, neutron star or a black hole) in a close binary system. Matter donated by the normal companion star is captured by the compact primary star generating the release of X-rays. There are three categories of X-ray binaries: low mass X-ray binaries, supergiant high mass X-ray binaries and transient high mass X-ray binaries. The distinction between high and low mass systems refers to the mass of the companion star. The transient high mass X-ray binaries are characterized by long quiescent periods separated by bursts of intense X-ray activity.

Mass transfer in X-ray binaries occurs via three possible methods: disk-fed accretion, stellar wind accretion or stream accretion. Disk-fed accretion implies the formation of a disk of captured material around the compact star and is thought to be the only viable accretion method for low mass X-ray binaries. Stellar wind accretion refers to wind material that is blown off of the companion star and captured by the compact primary star. Stream accretion entails the existence of a dynamic gas stream originating at the surface of the companion star that interacts with the compact star.

The X-ray binaries studied in my thesis contain a neutron star as the primary. Neutron stars are the only objects in the known Universe that require relativistic considerations to describe their internal structure. Although a complete description of the neutron star has not been achieved, they are characterized by their compactness (typically assumed to have a mass of ~1.4 $M_{\odot}$ and a radius ~10 km) and strong magnetic field (~10^{12} Gauss near the surface). The presence of such a strong magnetic field does not allow captured material to fall directly onto the surface of the neutron star. Rather, the material is funnelled along the magnetic field lines to the magnetic poles of the neutron star where an accretion column forms, transferring the captured material onto the surface of the neutron star. Radiation released during the accretion process is beamed away from the neutron star along its magnetic field axis. Misalignment of the magnetic axis and the rotation axis of the neutron star causes observable X-ray pulsations.

The first survey of X-ray sources was implemented by the satellite Uhuru in the early 1970's (Forman 1978). Since the pioneering work of Uhuru, many X-ray observing satellites have been placed in orbit, allowing the study of X-ray binaries. The Rossi X-ray Timing Explorer is an X-ray observatory that was launched in 1996. Aboard the Rossi X-ray Timing Explorer is an All Sky Monitor. This telescope surveys 80% of the sky every ninety minutes, recording the position and intensity of X-ray sources. The All Sky Monitor is comprised of three proportional counters (described in chapter four) sensitive to the energy range 1.5-12 keV.

The motivation of my thesis is to investigate the method of accretion in supergiant high mass X-ray binaries that contain a neutron star primary exhibiting an eccentric orbit. Four X-ray binaries that fit these criteria are chosen for study: 4U 1907+09, OAO 1657-415, GX 301-2 and 2S 0114+650. The eccentric orbit of the primary causes orbital variations in X-ray radiation generated by the capture of stellar wind. Using twelve years of X-ray observations from the All Sky Monitor aboard the Rossi X-ray Timing Explorer an orbital light curve is generated for each system. These observed light curves are compared to a model light curve of a system undergoing accretion in the form of strong stellar winds with the presence of a dynamic gas stream.

My thesis is comprised of the following chapters. Chapter two offers a review of the basics of X-ray binaries, focussing on supergiant high mass X-ray binaries. I end the chapter with a discussion of the orbital geometry of the selected X-ray binaries. Chapter three provides a detailed description of accretion, including the process in which the gas stream model is formulated. In chapter four I briefly discuss the components of the Rossi X-ray timing Explorer, in particular the All Sky Monitor. As well, chapter four includes an examination of the method in which the observed orbital light curves are created for each system. Chapter five contains the results of comparisons between the observed light curves and those generated using my theoretical wind and stream accretion model; special attention is paid to 4U 1907+09. Finally, chapter six includes a discussion of the results of this research as well as future work.

Chapter Two: Background

2.1 X-ray Binary Star Systems

Astronomical observations show that nearly half of the stars in the sky are part of a double or binary star system. In some of these systems the stars are barely in gravitational contact, essentially living out their isolated lives while in loose orbit of one another. For other binaries, the stars are locked in close quarters where the gravitational effects are violent, distinctly affecting the evolution of the binary system. Matter donated by one member of the system and captured by the other is a process called accretion. Accretion is an extremely energetic process that is responsible for most of the of X-ray radiation observed in the Galaxy (Blidsten et al. 1997). The label 'X-ray binary' covers the broad classification of binary systems that are bright in X-rays due to accretion. Ninety percent of Galactic X-ray sources belong to either high-mass X-ray (HMXBs) or low-mass X-ray (LMXBs) binaries (Rosswog, 2007, p.219). Both types of systems are thought to contain a compact object, either a neutron star or a black hole, accreting matter from a non-compact companion. As convention dictates the compact object in the system will be referred to as the primary star, and the other star as the companion. For the purposes of my thesis the primary star will be assumed to be a neutron star, thus allowing use of various timing analysis techniques to obtain fundamental orbital parameters of the system such as period and the location of the point of closest approach of the two stars.

2.1.1 Low Mass X-ray Binaries

LMXBs are host to either a neutron star or a black hole as a primary star and a main sequence star of less than 1.4 solar masses ($M_{\odot}$) for a companion. LMXBs are mainly found in the bulge and globular clusters of the Milky Way, regions of the galaxy that are predominantly home to older population stars. These locations for LMXBs support the idea that LMXBs are home to a slowly evolving low mass companion.

Unfortunately it is often difficult to observe an LMXB in the visible band because its spectrum is dominated by X-rays. The average photon energy for a LMXB is $h\nu \leq 5$ keV ,well inside the accepted X-ray band of the electromagnetic spectrum which is $100 \text{ eV} \leq h\nu \leq 1 \text{ MeV}$, where h is Planck's constant and ν denotes the frequency of the photon.

In a LMXB an accretion disk around the primary is the trigger for the release of observed highly energetic photons (Frank, 2002 p.152). The accepted evolutionary process that creates a LMXB begins with two main sequence stars with a relatively large separation. The more massive of the two stars evolves more quickly to the giant stage and eventually reaches a size such that the outer envelope is no longer gravitationally bound to the star. The evolved star begins to undergo a process called Roche lobe overflow which creates a stable accretion disk around the primary star. A more detailed description of Roche lobe overflow is found in chapter three.

2.1.2 Be-Transient Binaries

Nearly half of all known accreting pulsars are observed to contain a Be type star as a companion (Bildsten et al. 1997). Be stars are rapidly rotating massive stars in which the equatorial velocity is nearing the star's break-up velocity (Iye 1986). The rotation of the star creates an equatorial disk which accretes matter onto the primary star. The presence of the disk is confirmed by emission lines in the stellar spectrum that can only be attributed to a disk surrounding the supergiant star. The sudden accretion of a large amount of disk matter by the primary star releases a great deal of energy in the form of X-ray production. The time scale for the X-ray outburst indicates the formation of an unstable disk around the primary star that collapses rapidly depositing a large amount of matter on to the neutron star surface (Stella et al. 1986). The mechanism of accretion that triggers the X-ray release is chaotic, giving rise to the transient nature of Be-Transient X-ray binaries. Many of the Be-Transients were only discovered during a large X-ray production episode (Bildsten et al. 1997).

The accretion of matter from the disk onto the primary can be quite complicated, driven by such processes as exchange of angular momentum between disk and star and disk instabilities due to clumpy matter. The study of accretion disk physics in X-ray binaries is dominated by complex magnetohydrodynamic (MHD) models (Frank, 2002, p.80). My thesis will rely on Bondi-Hoyle accretion to describe the accretion luminosity due to stellar winds, ignoring complicating features such as X-ray radiation, magnetic or fluid effects. A complete discussion of Bondi-Hoyle accretion will follow in chapter three.

2.1.3 High Mass X-ray Binaries

High mass X-ray binaries (HMXBs) as the name suggests, contain a massive, early type (spectral class O or B) companion star as well as a compact primary. Nearly all HMXBs are found in star-forming regions of the Galaxy (Rosswog, 2007, p.226). There are about 130 known HMXBs in our Galaxy, predominantly found in the Galactic disk. Early type stars can have stellar mass greater than $10\,M_{\odot}$, which leads to a short life span.

Radiation pressure in supergiant stars creates a highly active upper atmosphere typically blowing off $10^{-7}\ M_{\odot}$/year in stellar wind, compared to the solar mass loss rate of about $10^{-14} M_{\odot}$/year (Rosswog, 2007, p.227). Capture of a fractional amount of the stellar wind from the companion star powers the observed accretion luminosity of HMXBs; details of the process will be described in chapter three. The typical photon energy from an HMXB is greater than a few keV. The X-ray luminosity is on the order of 10^5 solar luminosities ($L_{\odot}$) for the average HMXB (Frank, 2002, p.159). The purpose of my thesis will be to study the periodic nature of the accretion luminosity for HMXBs. Four different HMXBs containing a supergiant companion and neutron star primary are selected for investigation. The location of each selected HMXB target is shown in Galactic coordinates in Figure 2-1, where the origin denotes the center of the Galaxy. Each system is found in the Galactic disk.

Table 2.1 Selected HMXB systems

Name of System	Primary Star	Companion type
4U 1907+09	Pulsar	O8-O9 Ia*
GX 301-2	Pulsar	B2 Iae**
2S 0114+65	Pulsar	B1Ia‡
OAO 1657-415	Pulsar	B0-B6 Iab†

* Fritz, S. et al. A&A, 458:885-893, 2006
** Leahy, D. A., A&A, 391:219-224, 2002
† Bildsten et al. ApJ-supp., 113:367-408, 1997
‡ Levine & Remillard, ApJ, 656:431-436, 2007

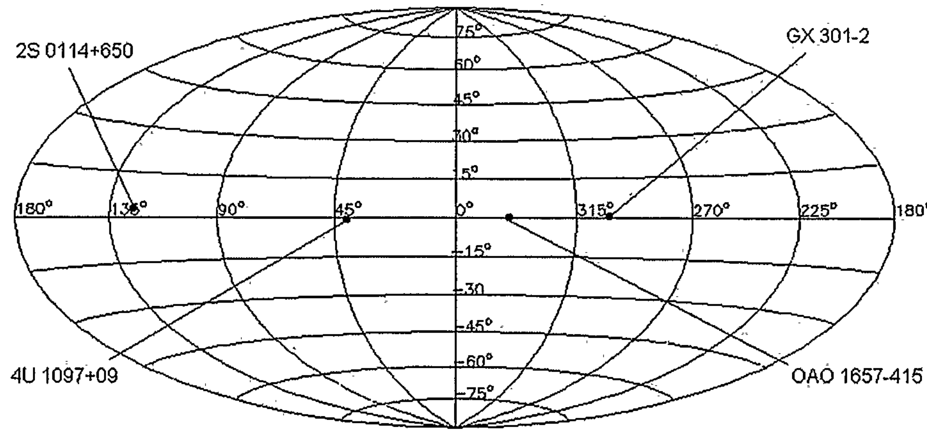

Figure 2-1 Galactic distribution of selected HMXBs plotted in Galactic coordinates. Note that each system is located within a few degrees of the midline of the Galactic disk.

2.2 Pulsars

While conducting her Ph. D. research studying radio emissions from quasars, Jocelyn Bell found regularly occurring "scruff" in her data (Hewish et al. 1968). Upon finer resolution of the scruff she found that it was made up of a series of radio pulses equally spaced 1.337 seconds apart (Carroll, 1996, p.604). The precision of the pulse intervals was unprecedented in astronomy of that era and led Bell and her supervisor Anthony Hewish to dub the findings LGM or *little green men*. Further scrutiny of their data revealed three other pulsating sources that appeared in different locations on the sky, each with a similar remarkably precise period (Hewish et al. 1968). With multiple sources of varying flux at different locations on the sky, the probability that the pulsations were attempts to hail Earth from distant civilizations fell to nil and the physical explanation of stable oscillations of either a white dwarf or neutron star was proposed (Hewish et al. 1968). Current astrophysical theory describes the origin of these radio pulsations to be rapidly rotating neutron stars. A sketch of a radio pulsar including magnetic field lines can be seen can be seen in Figure 2-2. Radio pulsars and X-ray pulsars are two different classes of rotating neutron stars.

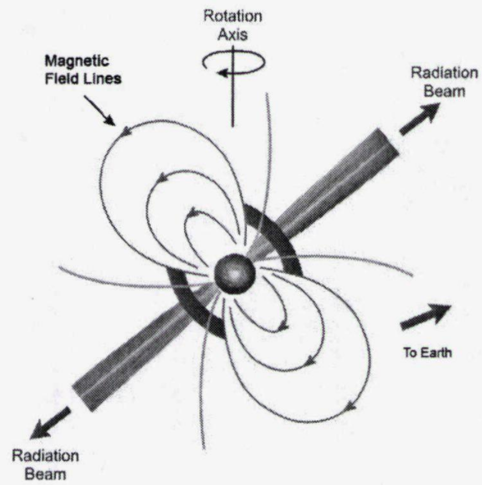

Figure 2-2 Schematic representation of Pulsar geometry. The misalignment of the magnetic or beaming axis from the rotational axis causes observed pulsations (Image from National Radio Astronomy Observatory; www.nrao.edu).

X-ray pulsars are powered by accretion from a companion star in a close binary orbit (Carroll, 1996, p.726). Stellar wind material captured by the neutron star is abruptly stopped by magnetic pressure before hitting the surface of the star. The accreted matter is funnelled along the magnetic field lines to the poles of the neutron star where it then falls onto the surface releasing energy in the form of X-rays. The pulsations which give rise to the pulsar's name occur when the magnetic axis of the neutron star is misaligned with the rotation axis. The X-rays released in the accretion process are beamed away from the neutron star along the magnetic axis. Each time the X-ray beam passes through the line of sight to the neutron star astronomers observe a pulse.

Shortly after the discovery of the neutron by Sir James Chadwick in 1932, the possible existence of a neutron star was proposed (Oppenheimer & Volkoff 1939). Since then there has been a great deal of theoretical work done to describe what might be typical characteristics for a neutron star. The progenitor of the neutron star is a massive star gone supernova (Carroll, 1996, p.514); the violent explosion of the star tears it apart leaving behind the tremendously dense stellar core. A unanimously accepted description of the structure of a neutron star has not been reached by the astrophysics community.

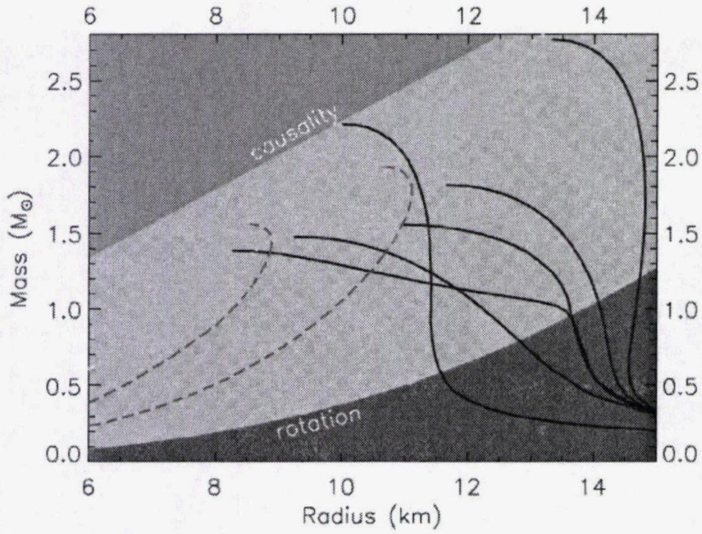

Figure 2-3 Mass vs radius diagram for a neutron star. The solid lines indicate equations of state for normal matter and dashed lines represent those of quark matter. Points that fall on a curve represent possible mass and radius values for the neutron star for the given equation of state. The forbidden regions are as well indicated (Lattimer et al. 2004).

The composition of a neutron star is agreed to have five major regions: the inner and outer core, the crust, the envelope and the atmosphere (Lattimer et al. 2004). The envelope and the atmosphere contain minimal mass but significantly affect the observed spectrum of neutron stars. The crust extends between one and two kilometres below the surface and predominantly contains matter in the form of nuclei. Within the crust however there is a point where the density exceeds the neutron drip density

($4 \cdot 10^{11}$ g cm^{-3}), when it becomes more energy efficient for matter to exist as free neutrons rather than in nuclei (Rosswog,2007, p.185). The core of a neutron star contains 99% of the star's mass (Lattimer et al. 2004). However, the equation of state that describes the interior of a neutron star remains a hotly debated subject in astrophysics.

To date there is no observational means to determine the structure of a neutron star, namely both the mass and radius simultaneously. Measurements of 50 radio pulsars in binary systems found that the observed neutron star masses fall within the narrow range of $M_n = 1.35 \pm 0.04 M_\odot$ (Thorsett & Chakrabarty 1999). Theoretical predictions of a neutron star's mass and radius are dependant on the equation of state chosen to describe the star. The curves plotted in Figure 2-3 describe several possible equations of state for a neutron star. Causality puts an upper limit on the mass of a neutron star for a given radius (Rhoades & Ruffini 1974). This causal limit ensures that the speed of sound in the neutron star remains lower than the speed of light. The maximum rotation speed (the mass shedding limit) constrains the allowable radii for a neutron star (Lattimer et al. 2004). Due to the extreme density, $\rho_{avg} \sim 10^{14}$ g cm^{-3} in the core of a neutron star possible strange matter physical descriptions exist (Prakash 2007). For calculations in my thesis I will assume the approximate values of 1.4 $M_\odot$ and 10 km for the mass and radius of a neutron star.

A defining feature of the neutron star is the inevitability of an exceptionally strong magnetic field. For an order of magnitude approximation of the strength of the magnetic field of a neutron star, consider the following *back of the envelope* calculation of resultant magnetic field (B_f) from the collapse of the Sun to a radius of 10 km (R_f)

assuming conservation of magnetic flux (ϕ) and an initial solar magnetic field on the surface of $B_i \approx 100\text{G}$.

$$\phi_i = \phi = \phi_f \qquad [2\text{-}1]$$

$$\int \vec{B}_i \cdot d\vec{a}_i = \int \vec{B}_f \cdot d\vec{a}_f$$
$$B_i \pi R_\odot^2 = B_f \pi R_f^2$$
$$B_f = 100\text{G} \cdot \left(\frac{6.9 \cdot 10^{10}\,\text{cm}}{1 \cdot 10^{6}\,\text{cm}} \right)^2$$
$$B_f \sim 5 \cdot 10^{11} G$$

As the progenitors of neutron stars have radii orders of magnitude larger than that of the Sun, one would expect the magnetic field of a neutron star to be orders of magnitude larger than the value obtained in equation [2-1]. A reasonable approximation for the surface magnetic field of a pulsar would be 10^{12} Gauss (Rosswog, 2007, p.194).

The model that I used in this analysis to approximate an HMXB system considers a capture radius defining a volume around the neutron star. Calculations show that any stellar wind material that encroaches within the accretion region is to be captured (discussed in chapter three). The equation for the capture radius (R_{acc}) is determined by equating the kinetic energy of a packet of stellar wind (mass *m)* with its gravitational potential energy with respect to the neutron star (mass M_n).

$$\frac{1}{2} m v_{rel}^2 = \frac{G M_n m}{R_{acc}} \qquad [2\text{-}2]$$

$$R_{acc} = \frac{2 G M_n}{v_{rel}^2}$$

Where G defines Newton's gravitational constant and v_{rel} is the relative velocity of the gas packet with respect to the neutron star. For this analysis typical values for the capture radius tended to fall between $1\,R_\odot$ and $10\,R_\odot$. Magnetic field strength drops off as $\frac{1}{r^3}$, thus the magnetic pressure at the boundary of the accretion region is negligible, several orders of magnitude less than impact pressure. For this reason the remainder of my thesis will ignore magnetic effects.

2.3 Supergiant Stars

The study of stellar evolution was made possible by the advent of the Hertzsprung-Russell (H-R) diagram. An H-R diagram describes the relationship between absolute magnitude, luminosity, spectral class and effective temperature of stars (see Figure 2-4). While the luminosity of a star is generated by the nuclear burning of hydrogen into helium in the core, the star is said to a Main-sequence star (Carroll, 1996, p.484). The length of time a star spends undergoing core hydrogen burning is dictated by the mass of the star; more mass implies more rapid exhaustion of hydrogen as a fuel. The pioneering work on the evolution of Main-sequence and post Main-sequence stars was done by Icko Iben Jr (1967). Iben (1967) described the tract along the H-R diagram that a star will travel over its lifetime as a function of stellar mass.

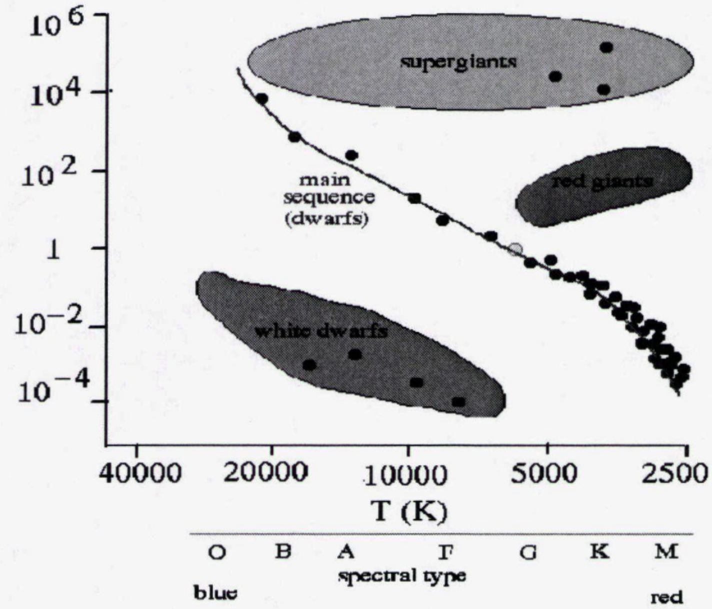

Figure 2-4 H-R diagram showing luminosity versus spectral class and effective temperature (Image from UCSD Center for Astrophysics & Space Science; cass.ucsd.edu).

For massive stars their life begins on the upper-left portion of the Main-sequence of an H-R diagram. After a massive star quenches the supply of hydrogen in its core a succession of nuclear reaction sequences occur, producing heavier and heavier elements through nuclear fusion (Carroll,1996, p.480). The nuclear burning takes place both in the core of the star as well as in concentric shells around the core. During this process the star cools moving it towards the right of the H-R diagram. If the star's Main-sequence mass was greater than ~8 $M_{\odot}$ the star will evolve into a supergiant star, (see Figure 2-4).

The HMXB systems chosen for this work were selected on the basis of having a massive supergiant companion star of early type, either O-type or B-type star (see Table 2.1). The radii of the companion stars are generally not well known although estimates show them to be nearly filling their Roche lobes, (Leahy 2002, Grundstrom et al. 2007 and Baykal et al. 2006).

The mass of the companion star in each system is not well known. In order to determine an expression for the companion star mass consider the reference frame in which the primary follows a Keplerian orbit about the companion which sits stationary at a focus of the neutron star's elliptical orbit (Rosswog, 2007, p.204). The systems studied in my thesis contain a pulsar as the primary star. This allows some insight into the orbit of the system, due to the fact that there should be regular X-ray pulses coming from the pulsar. Observations of pulsars in binary systems show regular lengthening and contracting of the pulse period due to Doppler shifting as the pulsar orbits its companion star (Chakarbarty et al. 1993, Koh et al. 1997). From Doppler analysis of the X-ray pulse arrival time astronomers are able to precisely determine the orbit of the HMXB. Knowledge of the orbital period of the HMXB allows us to calculate the mass function of the system, based on Kepler's third law,

$$\frac{G(M_c+M_x)}{a^3}=\left[\frac{2\pi}{P_{orb}}\right]^2 \qquad [2\text{-}3]$$

where M_x is the mass of the primary star, M_c is the mass of the companion, a is the semi-major axis of the orbit, G is Newton's gravitational constant and P_{orb} is the orbital period of the system. The *X-ray mass function* (f_x) is expressed as

$$f_x(M_x,M_c,i)=\frac{(M_c\sin i)^3}{(M_x+M_c)^2}=\frac{P_{orb}v_x^3}{2\pi G} \qquad [2\text{-}4]$$

where i denotes the inclination of the system. The *X-ray mass function* depends on observable parameters only, P_{orb} and v_x, where v_x is the velocity amplitude of variation.

Both observable parameters can be accurately determined by Doppler analysis of the pulse arrival times. Equation [2-4] can be rearranged such that

$$\frac{f_x}{(M_c \sin i)^3}\left[\frac{M_x}{M_c}+1\right]^2 - M_c = 0 \qquad [2\text{-}5]$$

Using a simple root finding algorithm under the assumption that the pulsar mass is $1.4 M_\odot$, equation [2-5] has reduced the companion mass to a function of a single orbital parameter, namely the inclination of the system (which will be defined in the following section). For the case in which the observed mass function (f_c) comes from optical observations of the companion star, the expression becomes

$$f_c(M_x, M_c, i) = \frac{(M_x \sin i)^3}{(M_c + M_x)^2} = \frac{P_{orb} v_c^3}{2\pi G} \qquad [2\text{-}6]$$

this yields an expression for the mass of the companion star

$$M_c = \sqrt{\frac{(M_x \sin i)^3}{f_c}} - M_x \qquad [2\text{-}7]$$

in which the mass of the companion star has been reduced to a function of one unknown, inclination (for a given neutron star mass).

2.4 Geometry of Binary System

As previously stated, the neutron star in a HMXB system follows Keplerian motion. The basic Keplerian orbit consists of one body tracing an ellipse as it orbits the other body which sits at one of the foci of the ellipse and the center of our coordinate system. In our systems the primary star travels in an ellipse around the companion. Observations made of binary systems rarely see the true geometry of the system but rather a projection of the orbit onto the plane of the sky, let this be the x-y plane, which is perpendicular to our line of sight. The binary orbit can be fully described in three dimensional space by four parameters: semimajor axis, eccentricity, inclination and longitude of periastron (symbolically: *a, e, i* and ω respectively). Figure 2-5 shows a schematic representation of the basic geometry of each of the selected HMXB systems.

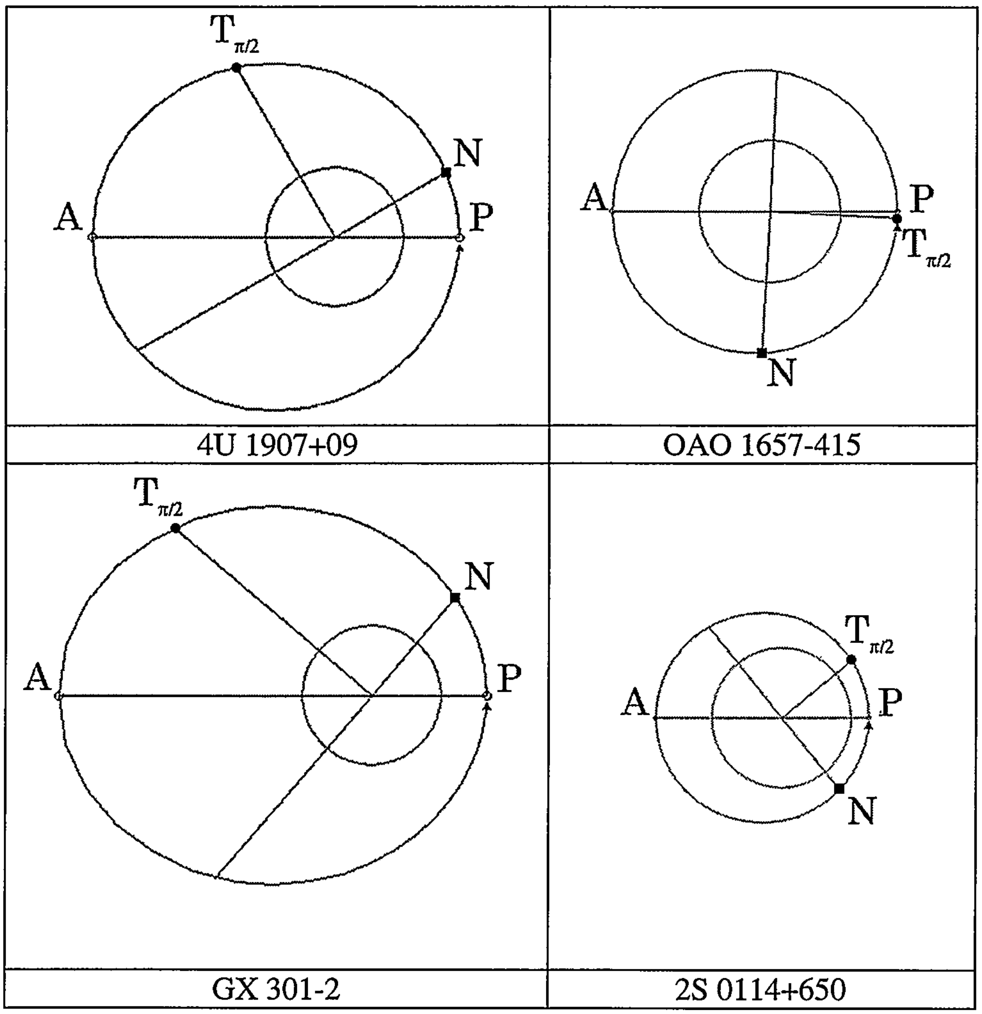

Figure 2-5 Schematic diagrams of the orbital system for each studied HMXB. For each system the assumed direction of orbit is counter-clockwise. The labelled values denote the following: A – apastron, P – periastron, N – location of the ascending node, $T_{\frac{\pi}{2}}$ - orbital epoch.

For a binary system, periastron passage (P) is the point of closest approach for the two stars, while apastron (A) corresponds with the maximum separation of the stars. The ascending node (N) of a binary system indicates the point in the orbit when the neutron star passes through the plane of the sky travelling away from the observer. The orbital epoch ($T_{\frac{\pi}{2}}$) of a binary is the time at which the neutron star has travelled ninety degrees from the ascending node. The ascending node defines the line of sight to the system, from which the system inclination (i) is measured. The inclination is the degree to which the system is inclined from the plane of the sky; an inclination of 0° implies the system is orbiting in the plane of the sky. While 90° of inclination would indicate that we are observing the system edge-on. The definitions of semi-major axis (a) and eccentricity (e) of the binary system come from the geometry of the orbital ellipse. The eccentricity of an ellipse is bounded by 0 and 1 and measures the departure from circular ($e = 0 \Rightarrow$ circle, $e = 1 \Rightarrow$ parabola). The semi-major axis is one half the longest axis of the ellipse, measured from the center through one of the foci of the ellipse. The semi-major axis as it is projected on the sky is denoted by $a \sin i$. The longitude of periastron (ω) is an angular measurement in the orbital direction of the neutron star from the ascending node to periastron. The basic geometry for a binary system is shown in Figure 2-6.

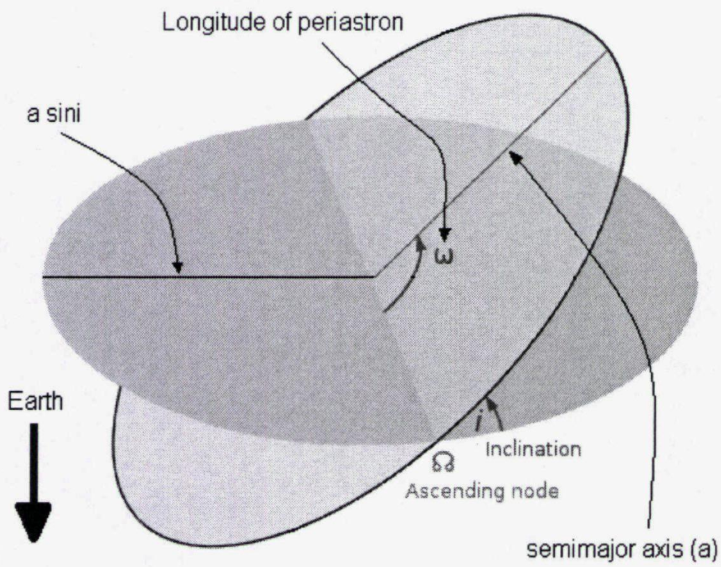

Figure 2-6 Sketch of geometry of binary orbit. The system inclination, location of the ascending node, longitude of periastron, as well as the projected and true semimajor axes are plotted, see the text for their definitions. The plane of the sky is perpendicular to the line of sight toward Earth.

Through Keplerian geometry, the longitude of periastron and the orbital epoch can be used to determine the time of periastron passage for a binary.

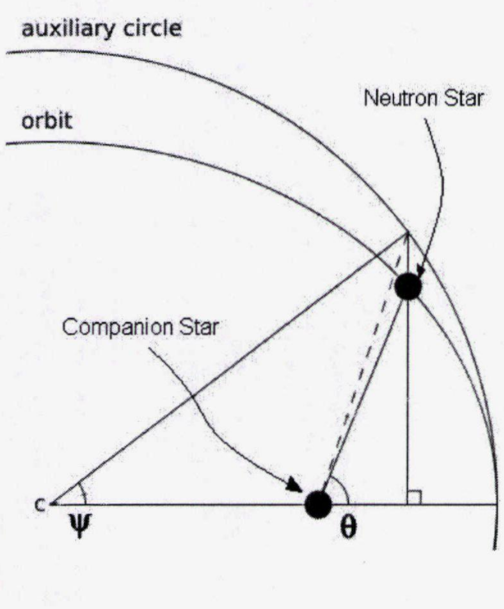

Figure 2-7 Geometry of an elliptical orbit, ψ denotes the eccentric anomaly and θ indicates the polar angle of the neutron star, C denotes the center of the ellipse (Image from Wikipedia, author: Lasunncty).

The eccentric anomaly (ψ), as seen in Figure 2-7, is an angular measurement of the position of a neutron star in an elliptic orbit which is related to the polar angle (θ) and eccentricity (e) of the orbit through the following equation

$$\tan\psi = \sqrt{\frac{1-e}{1+e}}\tan\theta \qquad [2\text{-}8]$$

In order to find the time of periastron passage we will consider the angular distance of periastron from the orbital epoch as $\theta = |\omega - 90|$. Using the system OAO 1657-415 as an example (mean longitude of periastron, $\omega = 93^{\circ}$ and eccentricity of 0.104)

$$\theta = 3^{o} \Rightarrow \tan\psi = \sqrt{\frac{1-0.104}{1+0.104}}\tan 3^{o} \qquad [2\text{-}9]$$

$$\psi = 2.703^{o} = 0.04718 \text{ rad}$$

The reason for using the eccentric anomaly is that there is an expression for motion in time (t) in a Keplerian orbit in terms of eccentric anomaly (Goldstein, 2002, p.98):

$$t = \left[\frac{\psi - e\sin\psi}{2\pi}\right]P_{orb} \qquad [2\text{-}10]$$

where P_{orb} denotes the orbital period of the system. Continuing with the example of OAO 1657-415,

$$t = \left[\frac{0.04718 - 0.104\sin 0.04718}{2\pi}\right]10.44809 \text{ days}$$
$$t = 0.07831 \text{ days}$$

the result of equation [2-10] implies that the neutron star takes 0.07831 days to travel from the orbital epoch to periastron. Using the measured value of orbital epoch ($T_{\pi/2}$) we can find an accurate value for the time of periastron passage (T_{peri})

$$T_{peri} = T_{\pi/2} + t \qquad [2\text{-}11]$$

$$T_{peri} = 48515.99 + 0.07831 \text{ MJD}$$
$$T_{peri} = 48516.06831 \text{ MJD}$$

The time of periastron passage will be used in the data analysis to create orbital light curves from observations collected by the Rossi X-ray Timing Explorer.

Table 2.2 Orbital Elements of Selected HMXBs

Source Name	Orbital Epoch[d] (MJD)	Periastron Passage* (MJD)	Orbital Period (days)	Inclination (deg)	Eccentricity	Longitude of Periastron (deg)	$a \sin i$ ($R_\odot$)	Mass Function ($M_\odot$)
4U 1907+09[a]	50134.76	50090.4462	8.3753(4)	57-80	0.28 ± 0.04	330 ± 20	35.8	7.9(21)†
GX 301-2[b]	48802.79	50130.726	41.498(2)	55-75	0.462(14)	310.4(14)	160	31.1(9)†
OAO 1657-415[b]	48515.99	50083.2818	10.44809(30)	≥ 60	0.104(5)	93(5)	45.7	11.7(2)†
2S 0114+650[c]	51825.3	50085.055	11.5983(7)	30-60	0.18 ± 0.05	51 ± 17	3.16	0.0032‡

[a] In't Zand, J. et al. ApJ, 496:386-394, 1998
[b] Bildsten et al. ApJ-supp., 113:367-408, 1997
[c] Grundstrom et al. ApJ, 656:431-436, 2007
[d] Orbital epoch is defined as the time in which the pulsar has travelled 90° past the ascending node
*Value derived from orbital epoch using mean longitude of periastron
†X-ray Mass Function
‡Optical Mass Function

Chapter Three: Accretion

At the heart of my thesis is mass transfer from the companion to the primary star, namely the process of accretion. The X-ray radiation from each binary system studied is a transformation of the gravitational energy of stellar wind material captured by the primary star (Bondi & Hoyle 1944). An order of magnitude calculation of the energy released (ΔE_{acc}) per unit mass from a parcel of matter, *m*, falling onto the surface of a neutron star of mass $M_n \approx 1M_{\odot}$ and radius $R_n \approx 10\text{km}$ shows the energy release of the accretion process, (*G* denotes Newton's gravitational constant)

$$\Delta E_{acc} = \frac{GM_n m}{R_n} \qquad [3\text{-}1]$$

$$\Delta E_{acc} = \frac{\left(6.67 \cdot 10^{-8}\,\text{dyne cm}^2\text{g}^{-2}\right)\left(1.989 \cdot 10^{33}\,\text{g}\right)m}{1 \cdot 10^{6}\,\text{cm}}$$

dividing by *m* to yield units of energy per unit mass

$$\Delta E_{acc} \sim 10^{20}\,\text{erg/g}$$

Comparing the energy released from this accretion process with that from the nuclear fusion (ΔE_{nuc}) of two parcels of hydrogen (each of mass $\frac{m}{2}$) to helium. The energy released in the nuclear fusion process is defined by the difference in mass of the initial and final species. From Frank (2002, p. 1) the equation describing the energy released in the nuclear fusion of hydrogen into helium looks as follows

$$\Delta E_{nuc} = 0.007mc^2 \qquad [3\text{-}2]$$

$$\Delta E_{nuc} = 0.007\left(2.99 \cdot 10^{10}\,\text{cm/s}\right)^2 m$$

dividing by m to yield units of energy per unit mass

$$\Delta E_{nuc} \sim 6 \cdot 10^{18} \text{erg/g}$$

where $0.007m$ denotes the amount less than m of resultant helium mass and c denotes the speed of light. Comparison of the results of equations [3-1] and [3-2] reveals that accretion on to a neutron star is nearly two orders of magnitude more energetic than nuclear fusion.

If we are to assume that all of the accretion energy is released as radiation then the X-ray luminosity (L_{acc}) from a primary star of constant mass (M_n) and radius (R_n) depends only on the rate ($\dot{m}$) in which the star accretes material, where G denotes Newton's gravitational constant.

$$L_{acc} = \frac{GM_n \dot{m}}{R_n} \qquad [3\text{-}3]$$

The sheer power of the accretion process puts an upper bound on the luminosity that it can release.

For very large values of luminosity the infalling stellar wind material can be blown away by radiation pressure, which effectively shuts off the accretion process. Another order of magnitude calculation will shed light on a typical value for the upper limit on accretion luminosity. This maximum is named the Eddington limit after the British astrophysicist, Arthur S Eddington. For the purpose of this calculation the accretion process will be assumed to be spherically symmetric and the rate $\dot{m}$ constant. The bulk of the accreted material in HMXB systems comes from the outer envelope of a main sequence companion star, thus a reasonable assumption is to consider the accreted material to be made up entirely of ionized hydrogen. For an accretion flow containing only free protons of mass m_p and electrons of mass m_e the radiative pressure acts mainly on the electrons. This is because the Thompson scattering cross section (denoted σ_T) of a proton is a factor of $\left[\frac{m_e}{m_p}\right]^2$ smaller than that of an electron or, $\sigma_T^{proton} \sim 3 \cdot 10^{-7} \sigma_T^{electron}$. The outward force on the electrons due to the radiation (F_{rad}) is found as

$$F_{rad} = \sigma_T \frac{S}{c} \tag{3-4}$$

where S is the radiant energy flux (units of erg/s/cm^2) and c is the speed of light. Although the accreting material is assumed to be completely ionized, the strong attractive Coulomb force acting between protons and electrons implies that electrons repelled by a radiative force act to drag protons away with them. In essence the radiative force tends to push outward against bound proton-electron pairs. Considering the net force (F_{net}) resulting from the inward gravitational pull (F_{grav}) on the accreting material and the outward radiative force

$$F_{net} = F_{grav} - F_{rad} \tag{3-5}$$

$$F_{net} = \frac{GM(m_p + m_e)}{r^2} - \sigma_T \frac{S}{c}$$

Defining the radiant energy flux in terms of luminosity (L) of the accreting source $S = \frac{L}{4\pi r^2}$ changes [3-5] to the following

$$F_{net} = \left[GM(m_p + m_e) - \frac{\sigma_T L}{4\pi c}\right] \cdot \frac{1}{r^2} \tag{3-6}$$

Thus the Eddington limit(L_{edd}) at which the outward force begins to dominate can be defined as

$$L_{edd} = \frac{4\pi GMm_p c}{\sigma_T} \qquad [3\text{-}7]$$

$$L_{edd} \sim 1.3 \cdot 10^{38} \left[\frac{M}{M_\odot} \right] \text{erg/s}$$

This calculation is valid for accretion of purely ionized hydrogen; the presence of other materials can alter the Eddington limit by a factor of ~2, by changing the ion mass per electron.

I will now delve deeper into the environment of HMXBs to lay the groundwork for a discussion of mechanisms of accretion.

3.1 Roche Geometry

The nineteenth century mathematician Eduardo Roche was the first to consider the gravitational field of a two body system during his work on planetary satellites. The process that Roche used is sometimes referred to as a restricted three body system because he considered the gravitational effects on a test mass in the presence of two massive bodies. The mass of the test particle was assumed to be negligible when compared to the other two masses and thus did not factor into the geometry of spacetime. Considering the orbit of the two masses to be circular about a center of mass, Roche derived what was to be known as the Roche potential, ($\Phi_R(\vec{r})$) which accounted for the gravitational and centrifugal forces of the binary system

$$\Phi_R(\vec{r}) = \frac{-GM_1}{|\vec{r}-\vec{r}_1|} - \frac{GM_2}{|\vec{r}-\vec{r}_2|} - \frac{1}{2}(\vec{\omega}\times\vec{r})^2 \qquad [3\text{-}8]$$

The first two terms yield the gravitational potential of each member of the binary system while the final term in the Roche potential considers the centrifugal force. The position of each star (M_1 and M_2) in the binary system is denoted by $\vec{r}_1$ and $\vec{r}_2$ respectively. The angular velocity of the binary system is denoted as $\vec{\omega}$ which in terms of the unit vector perpendicular to the orbital plane of the system ($\hat{n}$) looks as

$$\vec{\omega} = \sqrt{\frac{GM}{a^3}}\hat{n} \qquad [3\text{-}9]$$

where a denotes the semimajor axis of the system and M the total mass and G denotes Newton's gravitational constant.

Figure 3-1 displays two representations of the Roche potential of a binary system, one via a three dimensional plot and the other using a contour map. The two valleys near the center of the three dimensional plot represent the gravitational potential wells of the two stars in the system, while the overall convexity of the plot is due to the centrifugal force of the binary.

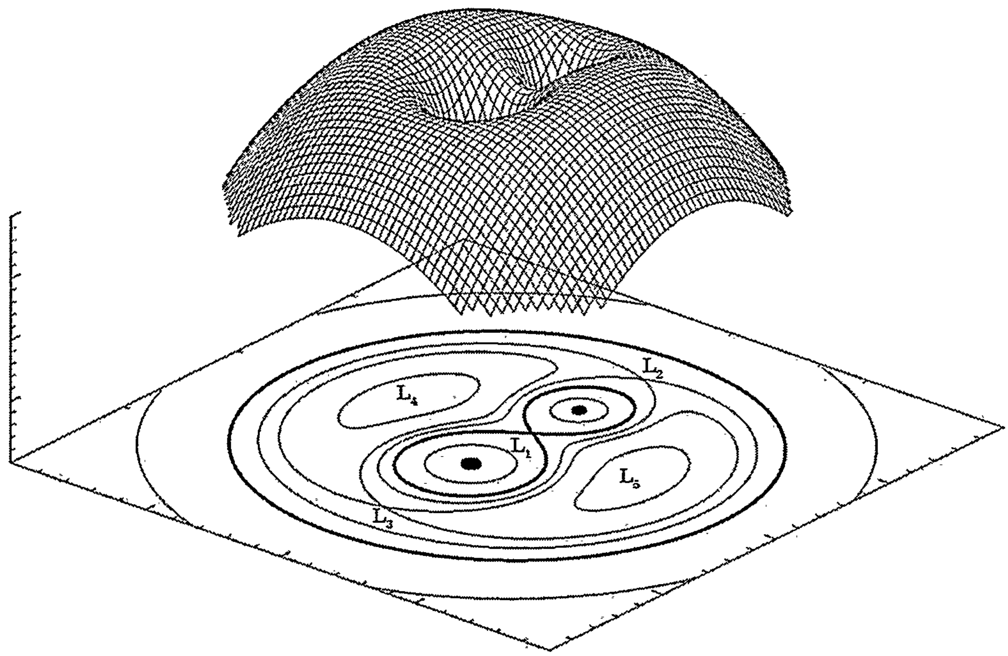

Figure 3-1 Roche geometry for a binary star system; the vertical axis measures the potential energy of the rotating binary and the horizontal axes are spatial dimensions. Above is a three dimensional representation of the distortion of spacetime caused by the two massive bodies. Below is a contour map of gravitational equipotential lines of the system, the five Lagrange points are labelled: L_1, L_2, L_3, L_4 and L_5 and the bold figure eight at the center denotes the Roche lobes of the system (Image from Wikipedia, author:I).

An important feature of the contour plot is the figure eight displayed in the bold which describes the Roche lobes of the binary. In essence a Roche lobe defines the cut-off within which all material is gravitationally bound to the star. The connection point of the two Roche lobes is labelled L1 and is the lowest stationary point of the system outside the potential wells of the stars. In this context a stationary or Lagrange point describes a point in spacetime where a small object could be a rest. In Roche geometry there exist five Lagrange points which are labelled in the contour plot of Figure 3-1. Clearly the Roche lobes are not spherical but can be characterized by an approximate radius that is dependant on the mass ratio of the stars and by the semimajor axis of the system (Eggleton 1983).

Mass transfer in binary systems most easily occurs through the L1 point. If during the lifetime of the star its radius exceeds that of its Roche lobe the L1 point acts as a very efficient means of mass loss, thus rarely will a star expand further than the radius of its Roche lobe (Friend & Castor 1982). Mass transfer of this variety is said to be due to Roche lobe overflow.

3.2 Disk Accretion

Consider a binary star system that contains a compact primary and a companion star that has evolved to completely fill its Roche lobe. For this system stellar material from the companion will be continuously spilling over the L1 point eventually to be captured by the primary (Frank, 2002, p.58). From the frame of reference of the primary star, material appears to be blasting inwards as if from a nozzle in rapid orbit about the star. Conservation of angular momentum does not allow the accreting material to fall directly onto the surface of the primary. Instead an accretion stream that originates from the L1 point begins to orbit the primary star, eventually interacting with itself (Owen & Blondin 1997). When the accretion stream collides with itself shocks and frictional forces act to heat up the accreting material removing energy in the form of radiation. The accreting material settles into a nearly circular orbit about the primary in the orbital plane of the system (this is an idealized situation; in reality the disk can be quite complicated, see Leahy 2004). The formation of an accretion disk allows viscous forces to transfer angular momentum radially outward within the disk. Eventually the innermost material has lost enough momentum to fall directly onto the surface of the primary star (neglecting magnetic effects).

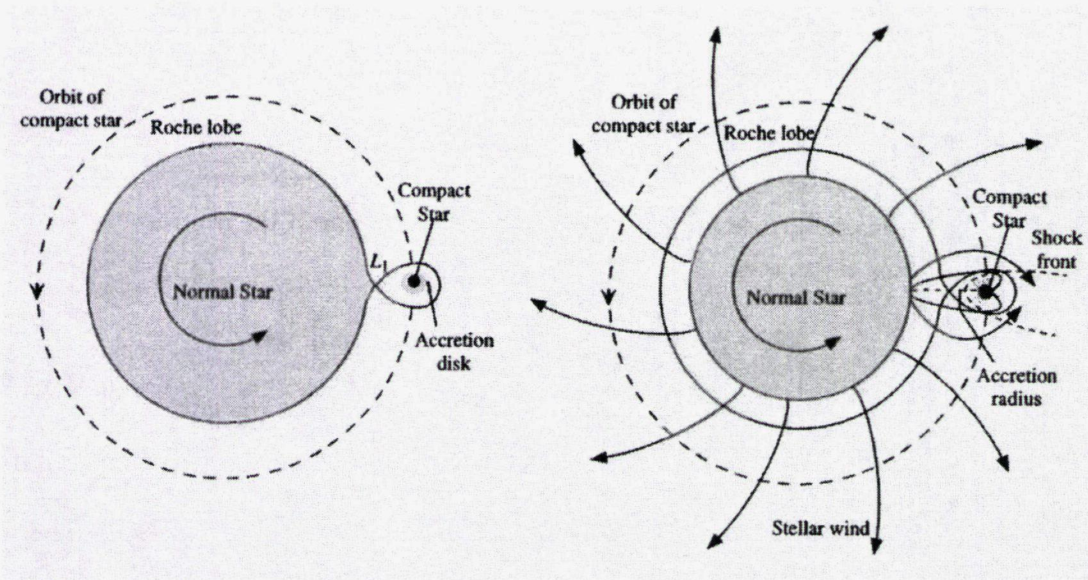

Figure 3-2 Mass transfer in binary system. Left: Roche lobe overflow. Right: Accretion due to strong stellar winds. (From Endo 2001)

The study of accretion disk physics dominates the discussion of accretion in astrophysics (Frank, 2002, p.80). My thesis will take a different tack and consider HMXB systems in which the accretion process does not include disks. For these systems the companion has not quite filled its Roche lobe and thus the mechanism of accretion is strong stellar winds (see Figure 3-2, right panel).

3.3 Wind Accretion

The radiation pressure in supergiant stars creates an active stellar atmosphere causing the release of large amounts of stellar wind (Castor et al. 1975). In a supergiant HMXB system some fraction of the stellar wind blown off by the companion will be captured by the primary star. As stated in equation [3-3] the accretion luminosity for a neutron star of fixed mass and radius would depend only on the rate at which the material is captured. The theory explaining the rate at which stars accrete material was first established by Bondi and Hoyle (1944).

In order to discuss Bondi-Hoyle accretion in more detail I will consider a HMXB system from the frame of the pulsar. From this frame of reference the stellar wind is travelling towards the pulsar with a velocity denoted as $\vec{v}_{rel}$.

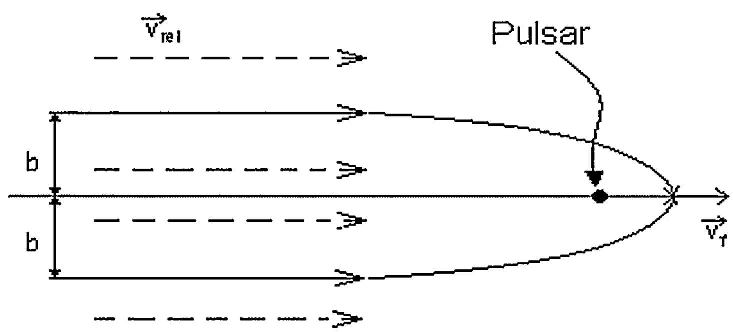

Figure 3-3 Sketch of stellar wind capture. The dashed arrows denote the direction of motion of the stellar wind. Two equal packets of wind material are forced to collide due to the influence of the neutron star's gravity. The resultant velocity ($\vec{v}_f$) of the new packet of wind material must be less than the escape velocity of the neutron star in order for the material to be captured.

Bondi-Hoyle accretion can be described by considering two equal parcels of stellar wind material travelling along a plane with parallel trajectories that are equal distances (b) away from the center of the pulsar (Edgar 2004). As the packets of wind material approach the pulsar they are influenced by gravity causing them to collide completely inelastically some distance behind, with respect to the origin of the stellar wind, the neutron star (see Figure 3-3). The new packet of stellar wind material is accreted if its resultant velocity ($\vec{v}_f$) is less than the escape velocity of the neutron star. For this process of accretion we can use the impact parameter b to define a circular surface area, $A_{acc} = \pi b^2$ for which all material that passes through is assumed to be accreted. The mass accretion rate follows simply by considering the density (ρ_{wind}) and velocity (v_{rel}) of the wind material that passes through the accreting surface.

$$\dot{m} = \pi b^2 \rho_{wind} v_{rel} \qquad [3\text{-}10]$$

In order to make use of $\dot{m}$ to calculate accretion luminosity it would be useful to express equation [3-10] as a function of stellar parameters and velocities. The square of the impact parameter b can be replaced by a function of relative velocity by considering the equations of motion of a packet of wind material as it is influenced by the neutron star's gravity.

To derive the equations of motion of the wind packet, I will first consider its lagrangian (L) which is the difference of kinetic (T) and potential (V) energy:

$$L = T - V \qquad [3\text{-}11]$$

$$L = \frac{1}{2}mv^2 + \frac{GMm}{r}$$

where v denotes the velocity of the wind packet (mass m) and r denotes its radial distance from the center of the neutron star. Newton's gravitational constant is denoted by G. In this system the gravitational attraction towards the neutron star (mass M) is the only source of potential energy. The equations of motion are best described in polar coordinates with the neutron star sitting at the origin, see Figure 3-4.

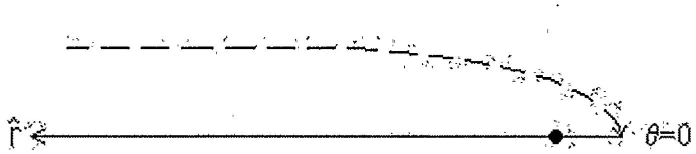

Figure 3-4 Trajectory of a single packet of wind material (dashed line). The location of the neutron star is denoted by the black dot, which corresponds with the origin of the system. Note that the angular component of position of the wind packet is zero on the right hand side of the neutron star along its midline.

Re-expressing the lagrangian in terms of polar coordinates:

$$L=\frac{1}{2}m\left(\dot{r}^2+r^2\dot{\theta}^2\right)+\frac{GMm}{r} \qquad [3\text{-}12]$$

where $\dot{r}$ and $\dot{\theta}$ denote the time-derivative of the radial and angular components of position of the wind packet. With the lagrangian as expressed in equation [3-12], Lagrange equations can be used to determine the equations of motion for a packet of wind material.

$$\frac{d}{dt}\left[\frac{\partial L}{\partial \dot{q}}\right]-\frac{\partial L}{\partial q}=0 \text{ where } q\in\{r,\theta\} \qquad [3\text{-}13]$$

First I will consider the angular component Lagrange equation, since the lagrangian does not depend on θ this implies

$$\frac{\partial L}{\partial \dot{\theta}}=const=h, \qquad [3\text{-}14]$$

which is a statement of conservation of angular momentum. With the assumption that the packet of wind material at a radial distance b from the neutron star it is still travelling with a velocity of v_{rel}, conservation of angular momentum states

$$r^2\dot{\theta}=bv_{rel}=h. \qquad [3\text{-}15]$$

Equation [3-15] will be used momentarily, but first attention must be paid to the radial component Lagrange equation, which is can be expressed as

$$\ddot{r} - r\dot{\theta}^2 = -\frac{GM}{r^2}. \qquad [3\text{-}16]$$

Using the substitutions $u = r^{-1}$ and $\dot{\theta} = \frac{h}{r^2}$ (from equation [3-15]), equation [3-16] can be re-expressed as:

$$\frac{d^2u}{d\theta^2} + u = \frac{GM}{h^2}. \qquad [3\text{-}17]$$

Equation [3-17] is a second order ordinary differential equation which has the general solution:

$$u = A\cos\theta + B\sin\theta + C \qquad [3\text{-}18]$$

The constants: *A, B* and *C* can be determined as follows. By substituting the solution (equation [3-18]) into the differential equation (equation [3-17]), the value for constant *C* is found to be:

$$C = \frac{GM}{h^2}. \qquad [3\text{-}19]$$

In order to find the constants *A* and *B,* I must consider the following boundary conditions. As a packet of wind approaches travelling in the $\theta = \pi$ direction the following two conditions must be true:

$$u \to 0$$
$$\dot{r} \to -v_{rel}$$

These boundary conditions are satisfied by the following expression for *u*:

$$u = \frac{GM}{h^2}(1 + \cos\theta) - \frac{v_{rel}}{h}\sin\theta. \qquad [3\text{-}20]$$

Equation [3-20] describes the radial position of a packet of wind material as a function of its angular component of position.

As described earlier, in order for stellar wind to be captured via Bondi-Hoyle accretion two equal packets of wind material must collide inelastically at the point $\theta = 0$, see Figure 3-4. The inelasticity of the collision of the wind packets of equal mass implies that there is no resultant azimuthal velocity for the new packet of wind material. Conservation of linear momentum dictates that the resultant radial velocity must be equal to v_{rel}. At the point $\theta = 0$ equation [3-20] simplifies to:

$$\mathrm{u} = \frac{2GM}{h^2} = \frac{1}{r}. \qquad [3\text{-}21]$$

For the new packet of wind material to be captured by the neutron star its kinetic energy must be less than the gravitational energy pulling it onto the neutron star:

$$T - V < 0$$
$$\frac{1}{2} v_{rel}{}^2 - \frac{GM}{r} < 0.$$

Using the expression for $\frac{1}{r}$ found in equation [3-21]

$$\frac{1}{2} v_{rel}{}^2 - \frac{2G^2M^2}{h^2} < 0.$$

Now I will make use of equation [3-15] which states $h = bv_{rel}$ and finally the square of the impact parameter can be expressed as a function of the relative velocity of the wind with respect to the neutron star:

$$b^2 = \frac{4G^2M^2}{v_{rel}^4}. \qquad [3\text{-}22]$$

Substituting equation [3-22] into the expression for $\dot{m}$ (equation [3-10]) yields:

$$\dot{m} = \frac{4\pi G^2 M^2 \rho_{wind}}{v_{rel}^3} \quad [3\text{-}23]$$

Since the stellar wind is smoothly moving radially outward at a speed of v_{rad} from the companion star conservation of matter implies

$$4\pi r^2 \rho_{wind} v_{rad} = const \quad [3\text{-}24]$$

$$\rho_{wind} = \frac{const}{4\pi v_{rad} r^2}$$

Thus with [3-24] I can re-express the rate of capture for Bondi-Hoyle accretion as

$$\dot{m} = \frac{\kappa G^2 M^2}{v_{rad} r^2 v_{rel}^3} \quad [3\text{-}25]$$

where κ is a constant. In order to account for the internal pressure of the wind I will replace the relative velocity by $v_{rel} \approx \sqrt{v_{rel}{}^2 + c_s^2}$ where c_s defines the speed of sound in the wind (Rosswog, 2007, p.227). Finally I am able to express the luminosity of Bondi-Hoyle accretion (see equation [3-3]) in terms of the neutron star mass, radius and position relative to the companion star (r) as well as the velocity of the wind.

$$L_{acc} = \frac{\kappa G^3 M_n^3}{R_n r^2 v_{rad} \left(v_{rel}^2 + c_s^2\right)^{3/2}} \quad [3\text{-}26]$$

While the neutron star mass and radius will be taken as constants the speed of sound is a function of the effective temperature, T_{eff} of the wind which is assumed to be a monatomic ideal gas, thus

$$c_s = \sqrt{\frac{\frac{5}{3} k_b T_{eff}}{m_{gas}}} \quad [3\text{-}27]$$

A discussion of the velocity of the wind will take place in the following section.

Despite the simplifications made by Bondi and Hoyle their work has stood the test of time and continues to make accurate predictions of accretion rates for several astrophysical situations including binary systems (Edgar 2004). Bondi-Hoyle accretion luminosity as derived in this section does not consider the effects of the primary star on the evolution of the stellar wind.

3.3.1 Radial Wind Velocity

The absorption and scattering of photons by the stellar wind material has been found to have a dominant effect on the evolution of material in the atmosphere of O and B type stars (Castor et al. 1975). The force due to absorbed and scattered radiation leads to an increase in the mass loss rate of early type stars of nearly one hundred fold compared to that which was previously predicted (Castor et al. 1975). The radiation force is found by solving the equations of radiative transfer under the assumption that there is a large velocity gradient in the wind, thus Sobolev's approximation holds which implies the effects of radiation can be determined locally. From this force, the radial velocity profile, v_{rad}, (henceforth referred to as the CAK profile) for stellar wind ignoring the Coriolis effect looks as

$$v_{rad} = v_{\infty}\left[1-\frac{R_c}{r}\right]^{\beta} \qquad [3\text{-}28]$$

where v_{∞} denotes the terminal velocity of the wind, R_c is the radius of the companion star, r denotes the radial distance of the wind from the center of the companion and β is a power law index that for the purpose of this thesis will be assumed to be unity (Roberts et al. 2001, Leahy 2002). This theory relies on spherically symmetric stellar wind however and cannot properly predict the orbital variability of the X-ray flux of HMXB systems which exhibit an eccentric orbit (Stevens 1988).

3.4 Stream Accretion

Until this point, the role of the primary star in the accretion process has been rather passive. The neutron star essentially defined the center of an accretion surface for which all material that passes through is assumed to be captured and the rest of the stellar wind material is considered lost from the system. Friend and Castor (1982) studied the effect of radiation-driven winds focussing their efforts on HMXB systems in which the companion nearly fills its Roche lobe. For this work they considered the effect of the primary star on the stellar wind. The assumption that the stellar wind is spherically symmetric is broken by considering the gravitational and radiative effects of the neutron star on the wind. These forces lead to a radical departure from the mass accretion rate predicted by spherically symmetric wind models (Friend & Castor 1982). Their work found that the asymmetry of the wind caused by the presence of the neutron star leads to an enhancement of the mass loss rate along the line of centers of the stars most prominent at periastron passage. Friend and Castor (1982) note the strong relationship between the ratio of companion star radius and Roche lobe radius and mass loss rate, suggesting that when the primary star is approaching periastron the mechanism of accretion resembles Roche lobe overflow more than stellar wind accretion.

The study of stellar wind-driven HMXB systems that exhibit an eccentric orbit had been unable to predict the short intense bursts of X-rays that occur near periastron because the models used relied on spherically symmetric stellar wind (Stevens 1988). An enhanced stellar wind accretion model for HMXBs in eccentric orbits (Stevens 1988) used the work of Friend and Castor (1982) to accurately predict the orbital variability of the X-ray transient A0538-66 which is known to have a highly eccentric orbit, $e = 0.7$ (Skinner et al. 1982). The conclusion of the work by Stevens (1988) was that the mass loss rate of the companion was increased near periastron passage yielding the observed peak in X-ray flux. Stevens (1988) hypothesized that a gas stream may be present in eccentric HMXBs. Stevens (1988) suggested that further study of the He II λ4686 (Gies & Bolton 1986) emission line along with the stellar wind calculations in his work could provide an accurate description of the behaviour of the stellar wind in A0538-66.

Based on the results of Stevens (1988) the possible presence of a gas stream in the HMXB GX 301-2 was suggested by Leahy (1991). Leahy (1991) compared accretion models containing three different types of gas streams along with strong stellar wind to observations of GX 301-2 from the TENMA satellite. The TENMA observations of GX 301-2 showed a large peak in X-ray flux just before periastron, which is common for X-ray binaries with eccentric orbits (Stevens 1988). The first gas stream model considered was that of a linear stream fixed in space near periastron. The stream was considered to be a density enhancement to the stellar wind, Gaussian in shape. The second model was identical to the first except that instead of being linear the center of the gas stream followed an Archimedean spiral. The third gas stream model had the same form as the first model but instead of being stationary the stream trailed the neutron star around its orbit. Statistical analysis done by Leahy (1991) showed that the preferential model of accretion was that of a stationary linear gas stream along with strong stellar winds. With the more complete data set obtained by RXTE-ASM compared to that from the TENMA satellite, the presence of a second less pronounced peak in X-ray flux near apastron was observed for GX 301-2 (Leahy 2002). The double flare structure of the orbital light curve indicated the likelihood of a single dynamic accretion stream present in GX 301-2 (Leahy 2002).

3.4.1 Dynamic Accretion Stream

Gravitational effects of the neutron star can create an accretion stream in the orbital plane of the HMXB system originating on the surface of the companion star along the line of centers of the binary (see Leahy 1991, Haberl 1991). In the model used in my thesis, the accretion stream is constructed as a linear interpolation of discrete gas packets that have been ejected from the companion star at equal intervals in time from the point on the surface of the companion that is closest to the neutron star. Before considering the accretion stream as a whole, attention must be paid to the evolution of the individual packets of gas.

Each packet of gas that makes up the accretion stream will be considered to be moving with the same velocity as the stellar wind. The radial component of the wind velocity (v_{rad}) is described by the CAK profile (equation[3-28]). Determination of the azimuthal component of wind velocity (v_{az}) can be done by considering conservation of angular momentum per unit mass

$$v_{az} r = v_{surf} R_c \qquad [3\text{-}29]$$

$$v_{az} = \frac{v_{surf} R_c}{r}$$

$$v_{az} = \frac{\omega_{surf} R_c^2}{r}$$

where R_c is the radius of the companion star, r is the radial position of the packet of gas and ω_{surf} denotes the angular velocity of the companion star. Since the angular velocity of the companion star in each of the selected HMXBs is not well known I will choose to describe it by the free parameter f_1 as

$$\omega_{surf}(f_1) = \omega_{\max} f_1 + (1 - f_1)\omega_{\min} \qquad [3\text{-}30]$$

The minimum angular velocity ($\omega_{\min}$) is defined as the average orbital velocity of the neutron star

$$\omega_{\min} = \frac{2\pi}{P_{orb}} \qquad [3\text{-}31]$$

where P_{orb} is the orbital period of the system. The maximum angular velocity ($\omega_{\max}$) is defined to be the periastron velocity of the neutron star which is dependant on the orbital period of the system and the eccentricity, e (Goldstein, 2002, p.96).

$$\omega_{\max} = \frac{2\pi}{P_{orb}} \frac{(1+e)^{1/2}}{(1-e)^{3/2}} \qquad [3\text{-}32]$$

Before creating the accretion stream as a linear interpolation of packets of gas, a derivation of an expression for the position coordinates of the gas packets in terms of time is required. This will be done for a coordinate system in which the companion star sits at the origin, beginning with the radial component. Consider

$$v_{rad} = \frac{dr}{dt} \qquad [3\text{-}33]$$

$$dt = \frac{dr}{v_{rad}}$$

where v_{rad} is described by the CAK profile plus the speed of sound in the gas (c_s). The inclusion of the speed of sound in the radial velocity is done to avoid division by zero at the point $r = R_c$. An integration of equation[3-33] follows using the integration variables $\tilde{r}$ and $\tilde{t}$:

$$\int_0^t d\tilde{t} = \int_{R_c}^{r} \frac{d\tilde{r}}{v_\infty\left[1-\frac{R_c}{\tilde{r}}\right]+c_s} \times \frac{\tilde{r}}{\tilde{r}}$$

$$t = \frac{1}{v_\infty}\int_{R_c}^{r} \frac{\tilde{r}d\tilde{r}}{\tilde{r}\left(1+\frac{c_s}{v_\infty}\right)-R_c}$$

let $x_1 = \frac{1}{1+\frac{c_s}{v_\infty}}$

$$t = \frac{1}{v_\infty}\int_{R_c}^{r} \frac{\tilde{r}d\tilde{r}}{\frac{\tilde{r}}{x_1}-R_c}$$

using the substitution $u = \frac{\tilde{r}^2}{x_1^2}$ yields

$$t = \frac{x_1^2}{2v_\infty}\int_{u_1}^{u_2} \frac{du}{\sqrt{u}-R_c}$$

which can now be integrated. Substituting back in for u and simplifying gives an expression for time in terms radial position, terminal wind velocity and the speed of sound

$$t = \frac{x_1^2 R_c}{v_\infty}\left[\ln\left(\frac{\rho - x_1}{1-x_1}\right)+\frac{1}{x_1}(\rho-1)\right] \qquad [3\text{-}34]$$

where ρ is the radial position in terms of the radius of the companion star. From equation[3-34] a root finding algorithm can be applied to give an expression for the evolution of the radial position of a packet of gas

$$\rho(t, v_\infty, c_s, R_c) = root\left[\left(x_1(x-1) + x_1^2\left\{\ln\left(\frac{x-x_1}{1-x_1}\right)\right\} - \frac{t \cdot v_\infty}{R_c}\right)\Big| x\right] \qquad [3\text{-}35]$$

where x is the variable that the root finding function solves for to give ρ. Now a similar procedure can be followed to find an expression for the evolution of the angular component of position of a packet of gas in the stream. Starting from the definition of angular velocity

$$\omega = \frac{d\theta}{dt} \qquad [3\text{-}36]$$

$$d\theta = \omega dt$$

$$\because dt = \frac{dr}{v_{rad}} \qquad \therefore d\theta = \frac{\omega dr}{v_{rad}}$$

Using conservation of angular momentum per unit mass to replace ω by $\omega_{surf}\frac{R_c^2}{r^2}$ an integration of the result of equation[3-36] looks as

$$\int_0^\theta d\tilde{\theta} = \int_{R_c}^r \omega_{surf}\frac{R_c^2}{\tilde{r}^2}\frac{d\tilde{r}}{v_\infty\left[1-\frac{R_c}{\tilde{r}}\right]+c_s}$$

$$\theta = \frac{\omega_{surf} R_c^2}{v_\infty}\int_{R_c}^r \frac{1}{\tilde{r}^2}\frac{d\tilde{r}}{1-\frac{R_c}{\tilde{r}}+\frac{c_s}{v_\infty}}$$

using the double substitution of $u = -\frac{1}{r}$ followed by $z = 1 + R_c u + \frac{c_s}{v_\infty}$ yields

$$\theta = \frac{\omega_{surf} R_c}{v_\infty} \int_{z_1}^{z_2} \frac{dz}{z}$$

Completing the integration and using the definitions of ρ and x_1 from the radial component derivation yields an expression for the evolution of the angular position (θ) of a packet of gas in the accretion stream

$$\theta(\rho, \omega_{surf}, v_\infty, R_c, c_s) = \frac{\omega_{surf} R_c}{v_\infty} \ln\left[\frac{\rho - x_1}{\rho(1-x_1)}\right] \qquad [3\text{-}37]$$

where ρ denotes the radial position of the packet of gas in terms companion radii, R_c, x_1 is a function of the speed of sound in the gas, c_s and the terminal wind velocity, v_∞ and ω_{surf} denotes the angular velocity at the equator of the companion star. Figure 3-5 shows the temporal evolution of the radial and azimuthal components of position for a gas packet in the accretion stream. Each packet of gas will evolve independently along a trajectory defined by equations [3-37] and [3-35], which can been seen in Figure 3-6. As stated previously, the accretion stream is comprised of a series of gas packets that have been ejected from the surface of the companion star along the line of centers in the binary. The radial component of the position of a packet of gas in the stream is entirely described by equation [3-35] and the angular component is found using equation [3-37] plus the ejection angle of the packet, which is determined by the orbital position of the primary star. For each instant in time a linear interpolation of the positions of gas packets defines the mid line of an accretion stream. The shape of the stream changes with time due to the eccentricity of the orbit of the neutron star.

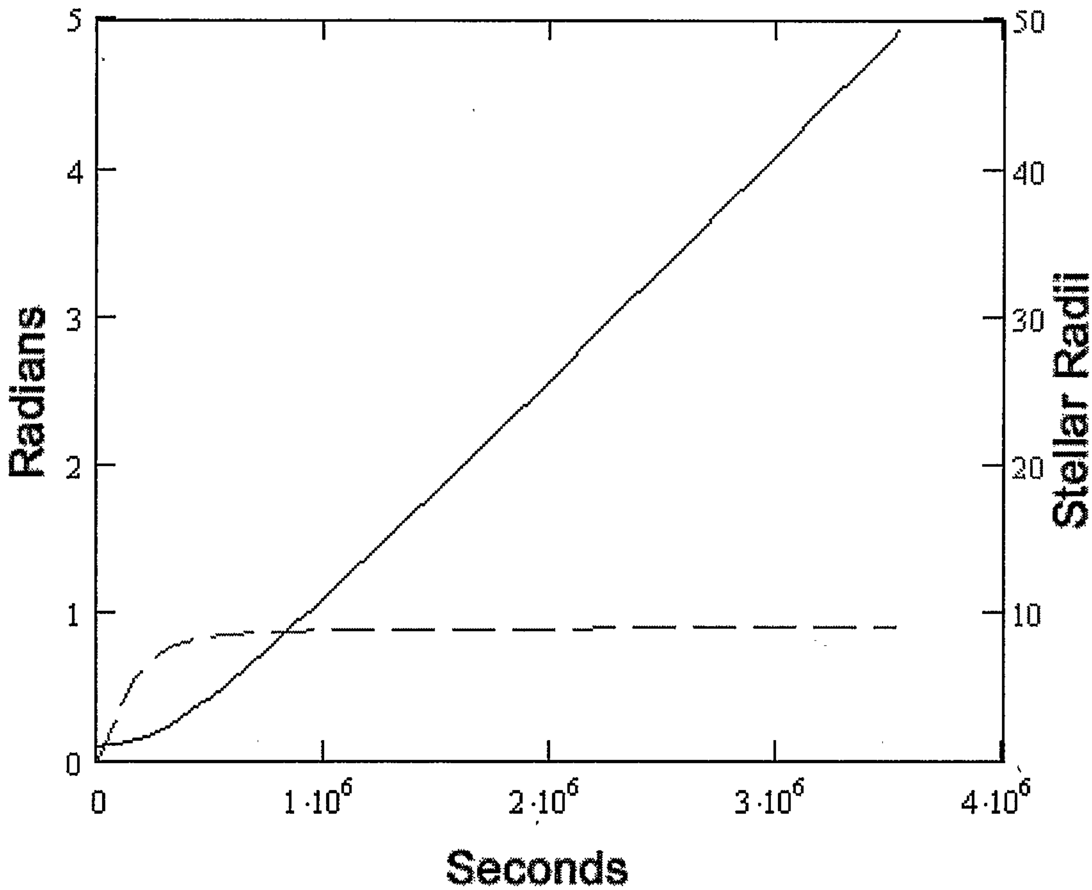

Figure 3-5 Evolution of gas packet in accretion stream. The solid line denotes the radial position and the dashed line shows the angular position. Plot is using best fit parameters for GX 301-2 with radius of 62 $R_{\odot}$ and inclination 60° (see chapter five).

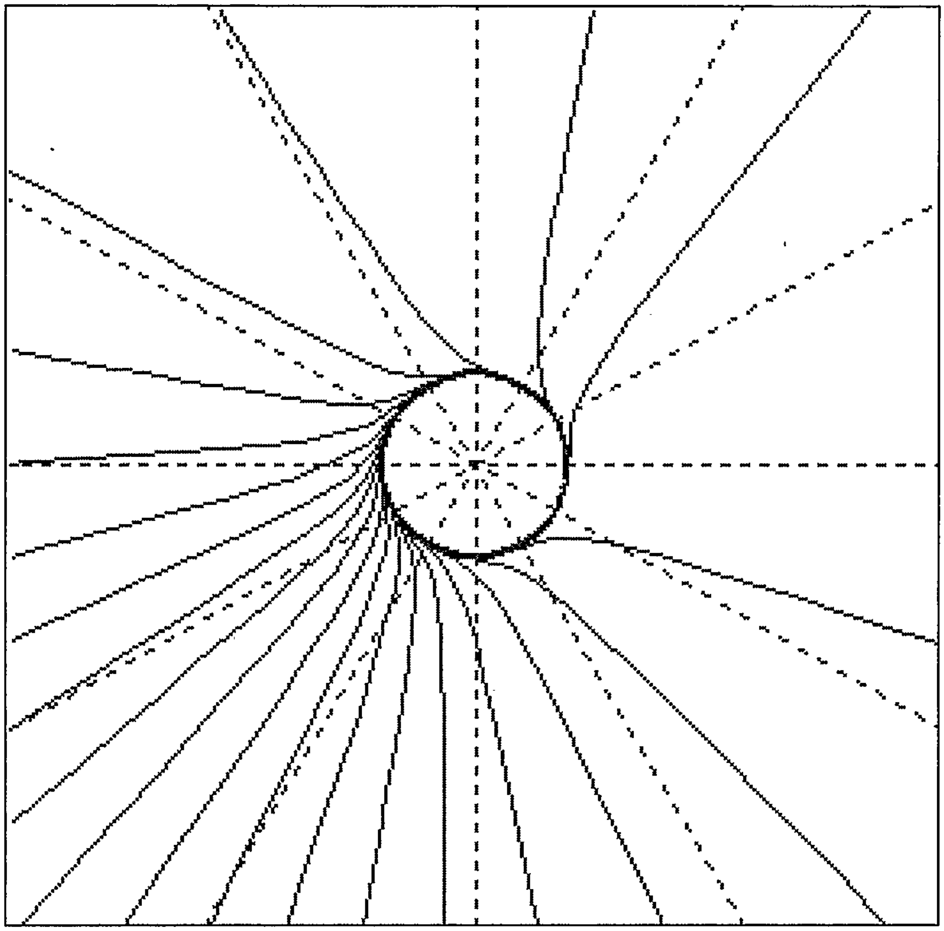

Figure 3-6 Trajectories of twenty gas packets spaced equally in time (solid lines). Plot is using best fit parameters for GX 301-2 with radius of 62 $R_{\odot}$ and inclination 60° (see chapter five). The neutron star is orbiting counter-clockwise for this diagram.

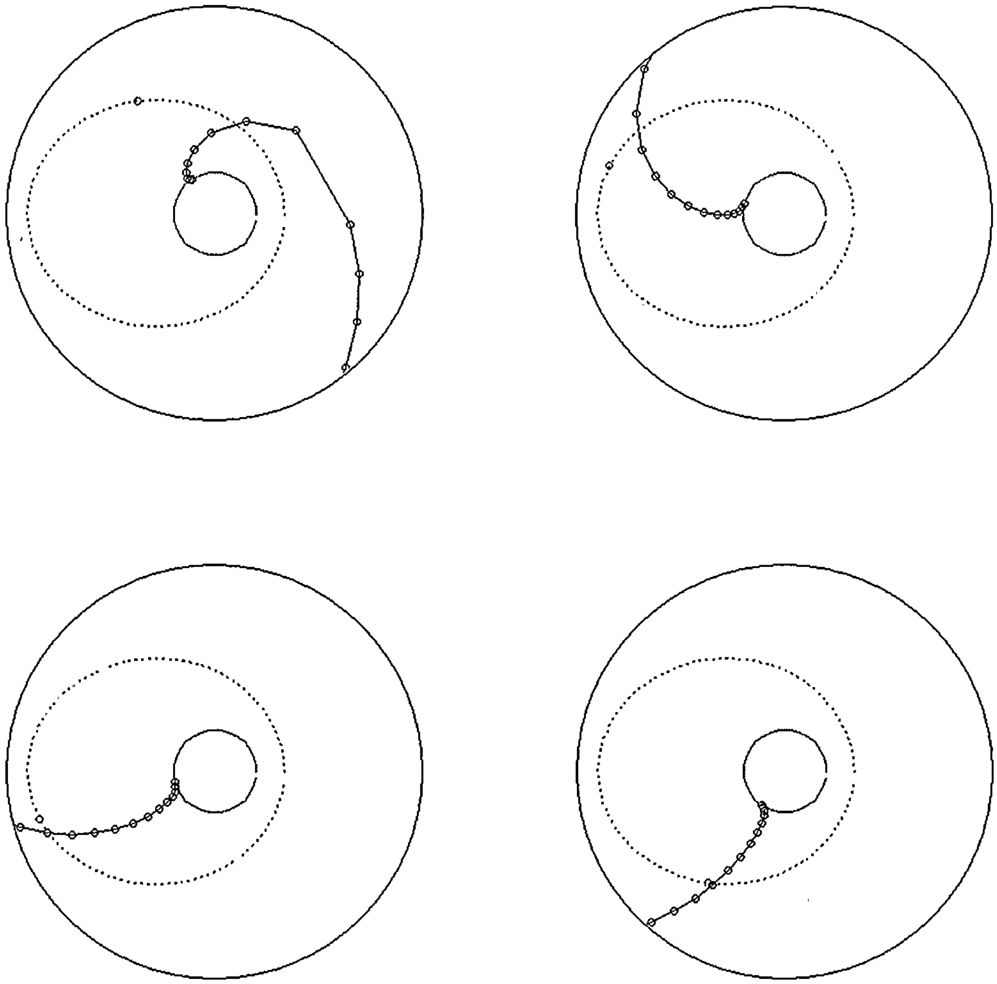

Figure 3-7 HMXB system GX 301-2 for companion radius $R_c = 62R_{\odot}$ and inclination 60°, including: accretion stream (solid line with circles), companion star (central circle), and the neutron star (small circle) on its orbit (dotted ellipse). Orbital phase 0.2, 0.4, 0.6 and 0.8, (top-left, top-right, bottom-left and bottom-right respectively).

Physically the accretion stream is a density enhancement to the stellar wind. In order to approximate the density profile, my model uses a Gaussian centered along the midline of the accretion stream. Previous work on the subject of stellar wind accretion with the presence of a density enhanced stream (Leahy & Kostka 2008) used a Gaussian in terms of angular units. The luminosity component due to the accretion stream (L_{stream}) was modelled as a Gaussian multiplied by the luminosity expected from Bondi-Hoyle accretion (L_{wind}, see equation [3-26]).

$$L_{stream} \propto L_{wind} \cdot d_s \cdot \exp\left\{\frac{-(\phi_{orb} - \theta_{cross})^2}{2\sigma^2}\right\} \qquad [3\text{-}38]$$

where d_s is the density enhancement factor, σ is the angular width of the accretion stream, ϕ_{orb} denotes the angular position of the neutron star and θ_{cross} represents the angular position of the intersection of the accretion stream and the neutron star orbit.

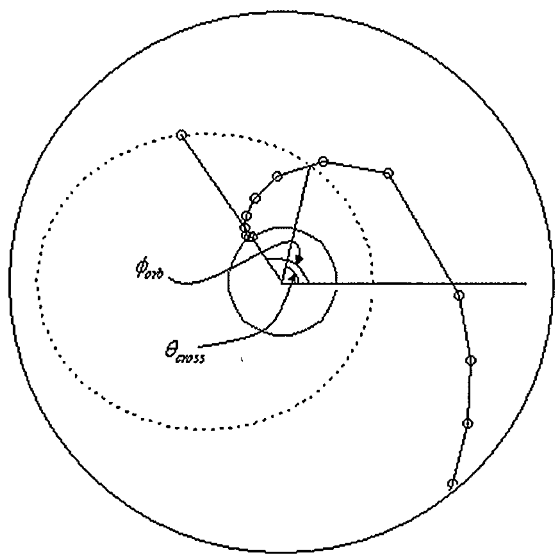

Figure 3-8 Gaussian accretion stream components for Leahy 2008 methodology. The plot includes: accretion stream (solid line with circles), companion star (central circle), the neutron star (small circle) on its orbit (dotted ellipse), ϕ_{orb} denotes the angular position of the neutron star and θ_{cross} denotes the angular position of the crossing point of the accretion stream and the neutron star orbit.

The research in my thesis is an extension of the work done by Leahy and Kostka (2008) modelling the X-ray light curve of GX 301-2. For my thesis the accretion stream is described in physical units and the new theoretical accretion model is compared to a selection of four HMXB systems. The following section will discuss the improvements I made to the Leahy and Kostka (2008) methodology that were implemented for the research of my thesis.

3.4.1.1 Current Methodology

This section outlines the accretion stream model that I created for my thesis research. I compared this model to the observed light curves of the selected HMXBs.

I varied the density of the accretion stream depending on the orbital location of the ejection point (ϕ_{ejc}) of each parcel of gas in the stream. Friend and Castor (1982) found that stellar wind accretion rate increased near periastron. To account for the periodic behaviour of the stellar wind accretion found by Friend and Castor (1982) the density of the accretion stream is modelled by the following sinusoidal function:

$$\mathrm{d}_{s1}(\phi_{ejc}, b) = \mathrm{d}_s\left[1 + b\sin\left(\phi_{ejc} + \frac{\pi}{2}\right)\right] \qquad [3\text{-}39]$$

where d_s is the density enhancement factor and b is a free parameter between zero and one that denotes the magnitude of periodic variability of the stream density.

To describe the width, $\sigma(w_o, v_{sp}, \tau)$ of the accretion stream in physical units I considered the stream to start from a non-zero initial width (w_o) and then expand at a constant speed (v_{sp}) as the material evolves along the stream.

$$\sigma(w_o, v_{sp}, \tau) = w_o + v_{sp} \cdot \tau \qquad [3\text{-}40]$$

Initial width and expansion speed of the stream are left as free parameters to be determined through statistical analysis, while τ describes the time that the point in question of the accretion stream has taken to evolve. The equation I used for the stream evolution time, τ was found during the derivation of the expression of the radial position of a packet of gas in the accretion stream (equation [3-34]).

For the stream accretion methodology of Leahy and Kostka (2008) the capture area around the neutron star was considered to be negligible. For my thesis a capture area surrounding the neutron star is considered. The orientation of the capture area is perpendicular to the direction of relative velocity of the stellar wind with respect to the neutron star. This capture area geometry is consistent with the definition of Bondi-Hoyle accretion (Edgar 2004). As previously stated, the accretion stream is approximated as a Gaussian shaped density enhancement to the stellar wind.

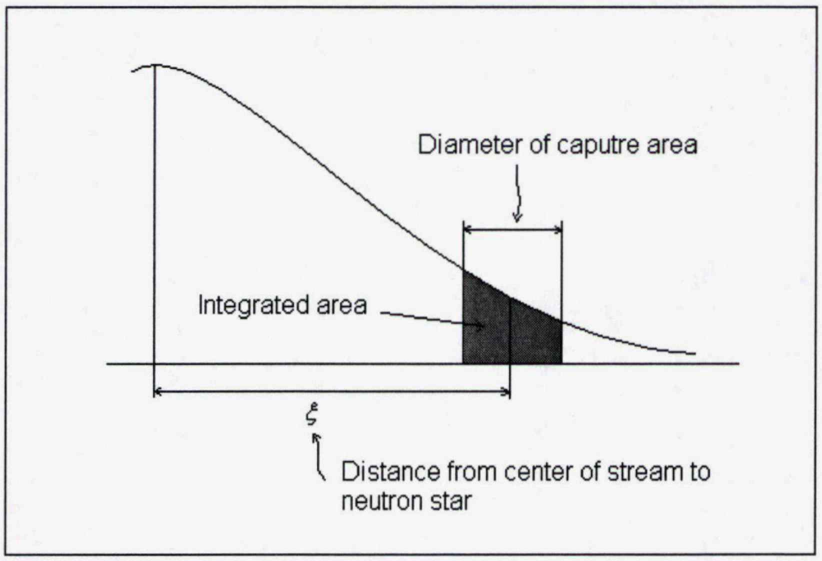

Figure 3-9 Schematic representation of the density profile of the accretion stream. The shaded area which is centered on the neutron star denotes the portion of the accretion stream that is captured.

In order to calculate the accretion luminosity contributed by the stream, the Gaussian must be integrated over the capture area. For simplicity, one-dimensional integration along the direction of Gaussian drop-off was considered.

Defining the direction in which the Gaussian dropped off proved to be a challenge. The first approach I considered was to define the Gaussian with respect to the orientation of the capture area. This implied measuring the separation of the neutron star and accretion stream along the line perpendicular to the relative velocity of the stellar wind and neutron star, see Figure 3-10.

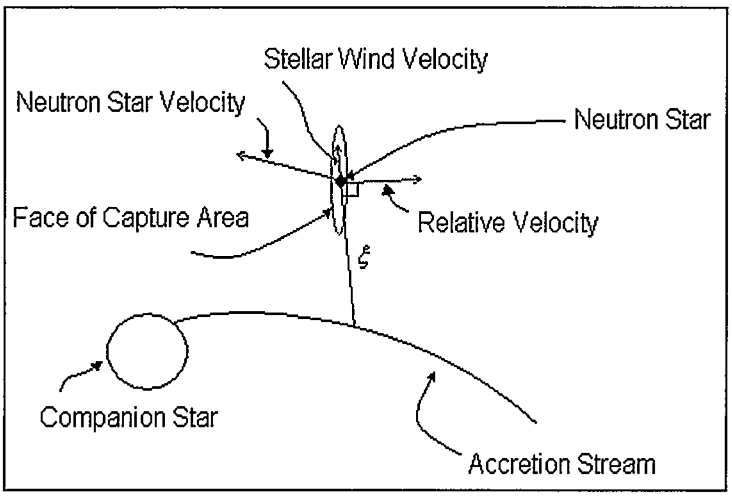

Figure 3-10 Orientation of capture area with respect to relative velocity of wind and neutron star. ξ denotes the distance from the neutron star to the accretion stream along the line perpendicular to the relative velocity of the stellar wind and the neutron star.

A problem arose with this distance measurement because the line defined by the direction perpendicular to the relative velocity of the stellar wind and neutron star did not cross the accretion stream at certain points of orbital phase for some systems. An alternate method for defining the direction of Gaussian drop-off of the stream had to be considered. The methodology I adopted was to assume that the stream density dropped off as a Gaussian in the direction perpendicular to mid line of the stream. The amount of accretion stream captured by the neutron star was calculated by integrating over an interval defined by the width of the true capture area, in the direction perpendicular to the accretion stream mid line, see Figure 3-11.

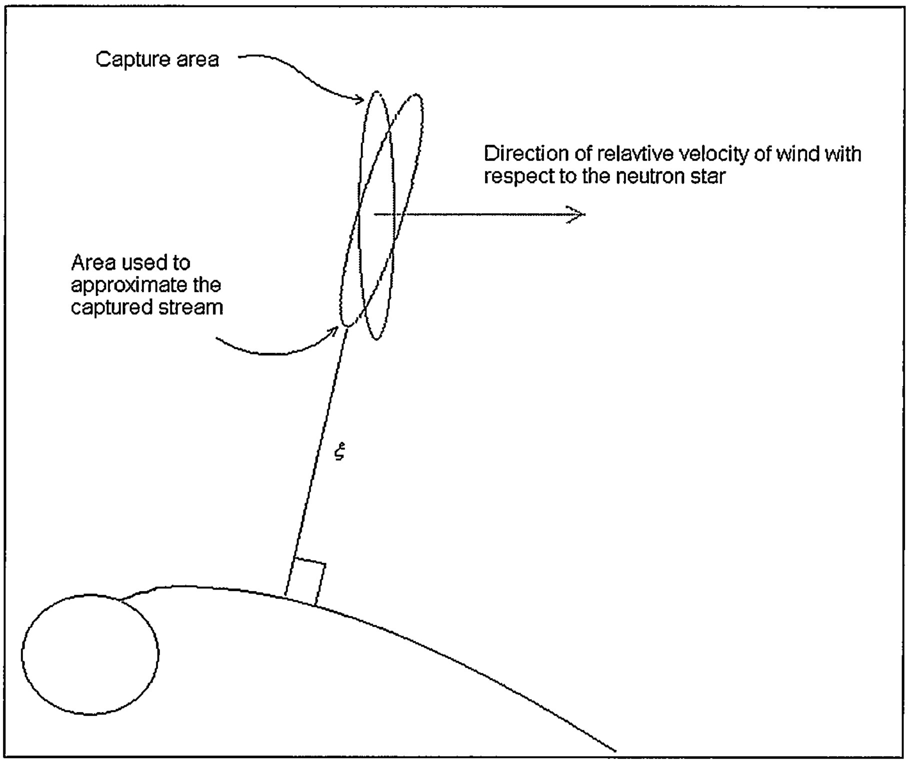

Figure 3-11 Approximation used to consider accretion from the gas stream.

The radius of the capture area (R_{acc}) is a function of the relative velocity of the stellar wind and neutron star (see equation [2-2]) found by equating the kinetic energy of a parcel of stellar wind material with the gravitational potential energy of the wind parcel with respect to the neutron star. In order to analytically account for the capture area in terms of luminosity I integrated the Gaussian representation of the accretion stream over an interval from r_n-R_{acc} to r_n+R_{acc}, where r_n denotes the radial position of the neutron star. The result is that the accretion luminosity of the stream becomes proportional to a difference of error functions rather than a Gaussian.

$$L_{stream} = L_{wind} d_{s1}(\phi_{ejc}, b)\sqrt{\frac{\pi}{2}}\frac{r^2 R_c}{\sigma(w_o, v_{sp}, \tau)}\left[erf\left(\frac{\xi + \frac{R_{acc}}{R_c}}{\sqrt{2}\frac{\sigma(w_o, v_{sp}, \tau)}{R_c}}\right) - erf\left(\frac{\xi - \frac{R_{acc}}{R_c}}{\sqrt{2}\frac{\sigma(w_o, v_{sp}, \tau)}{R_c}}\right)\right] \quad [3\text{-}41]$$

With the definitions of stellar wind and stream accretion luminosity derived in this chapter (equations [3-26] and [3-41] respectively) I am able to model the X-ray orbital light curves from HMXB systems. This model of the X-ray light curve from an HMXB exhibiting accretion via strong stellar wind and a gas stream originating at the surface of the companion star will be compared to the observed light curve of four HMXB systems. The X-ray binaries selected for comparison were chosen based on their non-zero eccentricity and the fact that the companion star in the system nearly fills its Roche lobe.

Chapter Four: Observations

4.1 Instrumentation

Observations used for analysis in my work come exclusively from the Rossi X-ray Timing Explorer (RXTE). The RXTE is a NASA satellite that was launched into a low Earth orbit on December 30th 1995 (Jahoda et al. 1996). Figure 4-3 displays a sketch of the RXTE satellite. The main scientific goal of the RXTE mission is to carry out study of the timing variability of X-ray sources. The satellite has moderate spectral resolution over a large energy range, 1.5-250 keV. The strength of RXTE is the timing resolution, which can resolve down to the microsecond scale. Aboard the RXTE satellite are three different instruments, the *Proportional Counter Array*, (RXTE-PCA), the *High Energy X-ray Timing Explorer*, (HEXTE) and the *All-Sky Monitor*, (RXTE-ASM).

The RXTE-PCA is an array of five proportional counters (see Figure 4-1 for a simplified diagram of a proportional counter) with a total collecting area of 6500 cm^2. In order for a detection to occur using a proportional counter an X-ray photon travels into a vapour-filled glass tube which collides with a particle releasing a high energy electron that in turn releases more low energy electron through collisions. The electrons are gathered by the central anode to create an electric pulse, which is interpreted as an X-ray detection. The main function of RXTE-PCA is to observe X-ray sources of moderate to low intensity, covering an energy range of 2-60 keV. The instrument is endowed with strong temporal resolution of approximately one microsecond and is the most sensitive of the three RXTE telescopes.

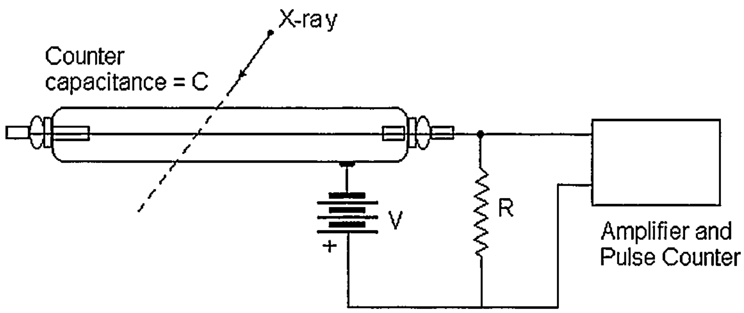

Figure 4-1 Schematic diagram of a simplified proportional counter.

The HEXTE instrument, as the name suggests, studies high energy X-rays from 15-250 keV. The telescope is made of two clusters of four scintillation counters (see Figure 4-2 for a schematic diagram of a scintillation counter), which are more efficient at absorbing high energy photons than a proportional counter. A detection occurs when the primary X-ray collides with scintillation crystal releasing a photon that hits the photocathode triggering the release of electrons. The electrons fall through a region of high voltage difference causing a cascade of electrons that eventually become an electric pulse that is measured by the counter. The full-width-half-max field of view of HEXTE is one degree. The ability to accurately measure high energy photons is made at a cost of sensitivity as HEXTE is only sensitive to flux down 5 keV. The timing resolution of the HEXTE is about eight microseconds.

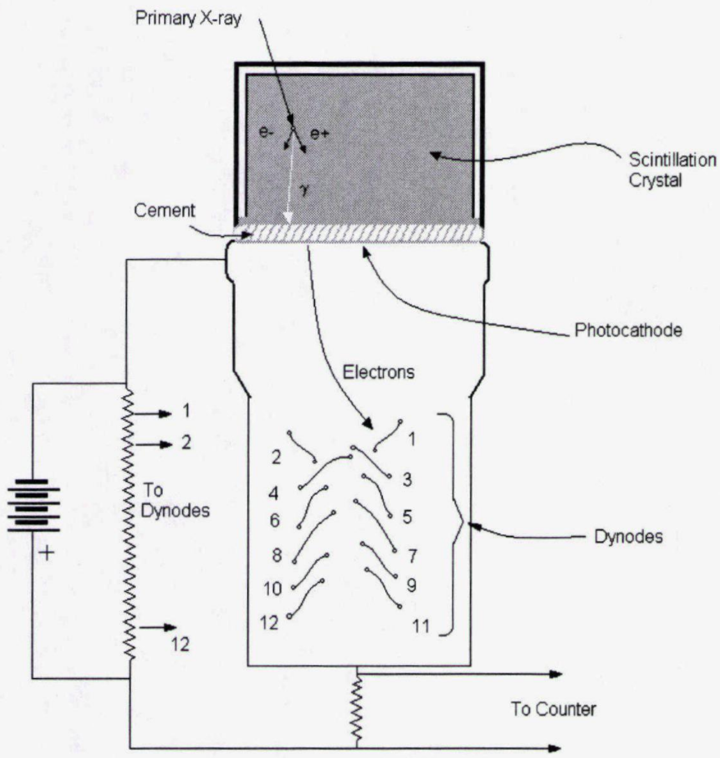

Figure 4-2 Schematic diagram of a scintillation detector.

4.1.1 Rossi X-ray Timing Explorer All-Sky Monitor

The RXTE-ASM is capable of scanning 80% of the sky every orbit, which can be done in as little as ninety minutes (Levine et al. 1996). The instrument is made up of three scanning shadow cameras (SSCs) sensitive to the energy range 1.5-12 keV at a moderate spatial resolution of 3' x 15'. The SSCs have a 6° x 90° field of view and the entire RXTE-ASM apparatus is able to be rotated about a central axis. Each SSC has an on-axis effective area of 10 cm^2, 30 cm^2 or 23 cm^2 at 2 keV, 5 kev or 10 keV respectively, giving the RXTE-ASM approximately 90 cm^2 of collecting area. RXTE-ASM is sensitive to flux as low as 30 mCrab. Figure 4-4 displays a schematic diagram of RXTE-ASM, including the dimensions of a single SSC.

Each of the SSCs that make up the All-Sky Monitor contains a position sensitive proportional counter (PSPC). The PSPC measures the displacement and strength of the shadow pattern cast by an X-ray source in the field of view (Levine et al. 1996). The position of the X-ray event is found using a slit mask that sits atop each PSPC, which has an energy dependent positional resolution between 0.2 mm and 0.5 mm. Each PSPC is guarded by a plastic thermal shield and surrounded by twelve metal anodes that are used to reject false detection events caused by charged particles. The PSPCs each contain eight resistive carbon-coated anodes that have their own dedicated electronic measurement chain. An X-ray event that is detected in the volume surrounding an anode produces two electronic pulse height signals; one is used in the charge division technique along with the slit mask to determine the position of the source and the other is used to interpret the strength of the signal (Levine et al. 1996). X-ray events measured by RXTE-ASM are channelled through event analyzers that are part of the onboard Experiment Data System (EDS). The data analysis done by the event analyzers bins the X-ray events via two separate criteria, position and which sub-band the photon energy falls into: 1.5-3 keV, 3-5 keV or 5-12 keV. The position histograms are accumulated in a series of approximately ninety second *dwells* during which the spacecraft maintains a steady attitude and the RXTE-ASM is refrained from being rotated.

For the purpose of my thesis observations from the RXTE-ASM are used for each selected HMXB. The full RXTE-ASM data set for each system is analyzed in the total energy band as well as each sub-band.

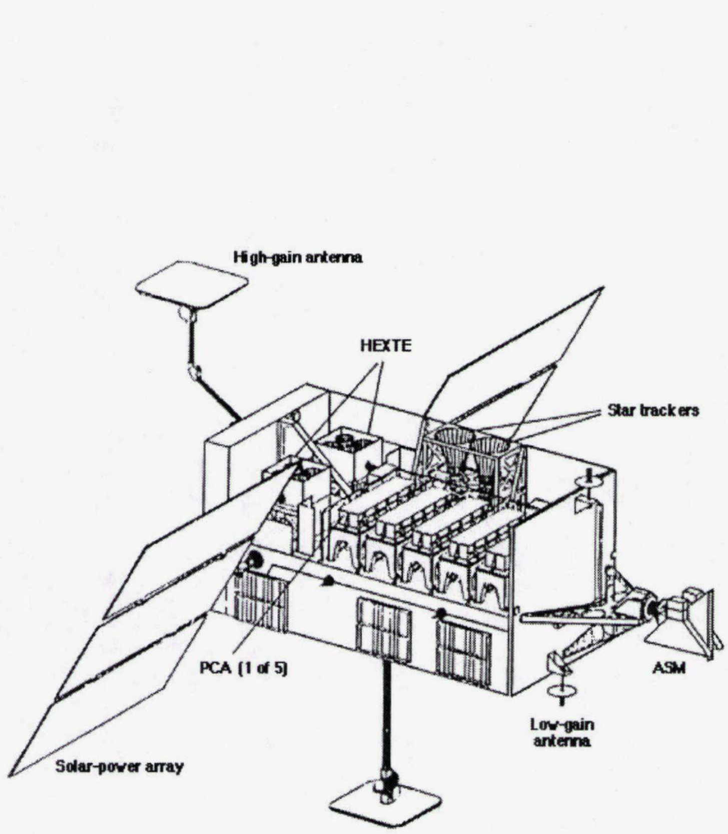

Figure 4-3 Rossi X-ray Timing Explorer. The relative positioning of each instrument aboard the satellite can be seen from this figure. (From NASA website: heasarc.gsfc.nasa.gov/docs/xte/)

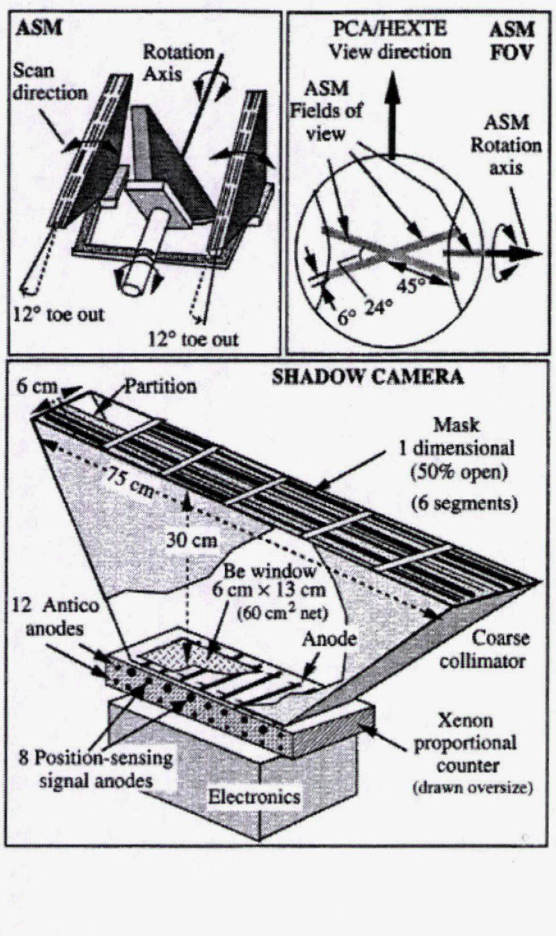

Figure 4-4 Upper left panel shows the set up of the RXTE-ASM along with the scanning direction and the axis of rotation. Upper right panel display the field of view for RXTE-ASM. The lower panel is a detailed schematic of one of the three scanning shadow cameras that make up RXTE-ASM (From Levine et al. 1996).

4.2 Data Analysis

The study of mass accretion in HMXBs is made difficult by the high variability of the process. One method of modelling accreting HMXB systems is through N-body simulations that must be run on supercomputer clusters. Code such as the Smoothed Particle Hydrodynamics (Lajoie & Sills 2008) or other magnetohydrodynamic codes (Owen & Blondin 1997) model the complexities of mass accretion in binary systems. Work of this detail is beyond the scope of my thesis. Rather than creating visual simulations, I will focus on the physics of HMXB systems. My research entails creating models of HMXBs and comparing them to X-ray observations.

A benefit of using data from the RXTE-ASM for analysis is the large time sample available as well as the continuity of observation. On average a given X-ray source has been observed five to ten times per day for the last thirteen years by RXTE-ASM (Levine et al. 1996). This is thanks to the large spatial coverage of RXTE-ASM as well as the low Earth orbit of the satellite.

My analysis will make use of the fact that RXTE-ASM has between one hundred and one thousand orbital periods observed for each selected HMXB. By using an epoch folding routine we are able to obtain a good average of the orbital X-ray light curve for each HMXB from the RXTE-ASM observations. The light curve obtained for each system is used in comparison to a model of a HMXB undergoing strong stellar wind along with a dynamic gas stream as a method of mass transfer.

4.2.1 Epoch Folding

The method used to create the orbital light curves is called epoch folding for which a computer algorithm was written by Denis Leahy. The folding program takes RXTE-ASM dwell data as an input and as an output yields X-ray count per second as a function of orbital phase for the selected HMXB. The process begins by choosing the number of partitions in phase the light curve will consider. For my analysis I decided to divide the orbital phase into forty equally spaced time intervals, with phase point zero corresponding to the moment of periastron passage for the HMXB. Using the date of the last periastron passage of the primary star as a reference point the epoch folding routine reads through the time stamps provided in the RXTE-ASM data chronologically, assigning each measured X-ray event to the appropriate phase bin. The epoch folding code as well contains error analysis which determines a value for the error associated with each phase point of the light curve. Using the epoch folding process I created sets of orbital light curves for all four of the HMXBs considered in my thesis. For each HMXB system analyzed in my thesis an orbital light curve was created from the total energy band observations of RXTE-ASM as well as from each of the aforementioned sub-band observations created by the EDS onboard analysis of RXTE-ASM. Visual comparison of the orbital light curves from each sub-band shows that there is no discernable signal coming from the lowest energy sub-band of RXTE-ASM for any of the HMXB systems (see Figure 4-5). The 1.5-3 keV band seems to be providing only noise to the total orbital light curve. Since HMXB systems tend to have high column density absorption of the lower energy X-ray photons could explain the large amount of noise observed by RXTE-ASM's lowest energy sub-band (Blidsten et al. 1997). For the reason that the 1.5-3 keV energy band contributes only noise to the orbital light curve of each HMXB system it was neglected from the statistical analysis of my thesis.

A benefit of the long life of RXTE-ASM is that it has allowed a long term continuous study of these HMXB systems, while a drawback is that as the satellite ages it begins to degrade. In their joint H-α, X-ray analysis of the system 2S 0114+650, Grundstrom et al. (2007) note that there appears to be a trend in the observations coming from one camera in RXTE-ASM of unknown origin. Further investigation by Dr. Levine and his team at MIT leads them to the conclusion that the camera is experiencing a slow gas leak (personal communication with Dr. Levine). The outgassing is influencing the voltage gain used to convert photon energy into pulse height in the affected camera, labelled SSC1 (Grundstrom et al. 2007). The issue is causing the problematic camera to measure a higher than expected number of photons registering in the 5-12 keV range. Data analysis by the RXTE research group at MIT works to reduce this error in the observations before they are released to the scientific community.

In order to test the effect of the troubled SSC1 an orbital light curve was created for the system 2S 0114+650 with the observations from said camera removed from the data set. Comparison of 2S 0114+650 light curves created with and without observations from SSC1 shows negligible difference in measured count rate. This process was repeated for each system, again showing insignificant divergence between the light curves produced with and without the observations from SSC1. We conclude that the gas leak in SSC1 is not causing a significant issue with the RXTE-ASM observations for the purpose in my thesis.

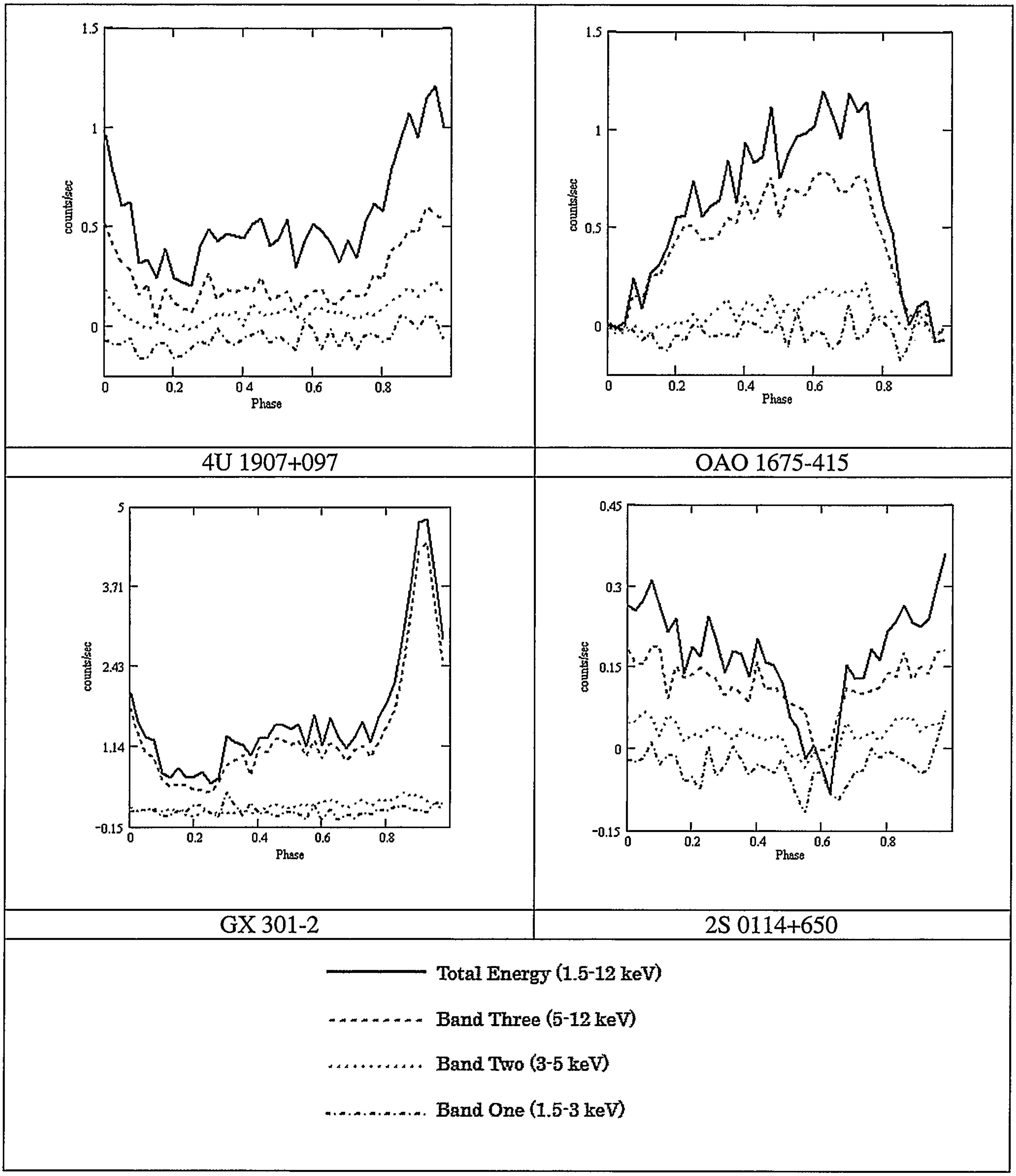

Figure 4-5 Orbital X-ray light curve for selected HMXBs created from RXTE-ASM data.

Chapter Five: Results and Analysis

The analysis in my thesis compares observations from RXTE-ASM to models of HMXBs powered by accretion from strong stellar winds and a gas stream. From this comparison I aim to achieve a realistic model for the selected HMXB systems. The statistical analysis utilized for my research is chi-squared (χ^2) minimization, which provides a measure of the goodness of fit between the model and observations. The definition of chi-squared is

$$\chi^2 = \sum_{i=1}^{40} \frac{[L_{obs}(i) - L_{theor}(i)]^2}{\sigma(i)^2} \qquad [5\text{-}1]$$

where $L_{obs}(i)$ is the observed light curve created from RXTE-ASM data, $\sigma(i)$ is the measurement error and $L_{theor}(i)$ is the theoretical light curve from our model. A routine is run that minimizes the chi-squared and yields values of the free parameters that give the best fit of the model to the observations for a given set of fixed parameters. The mass and radius of the companion were chosen as fixed parameters for the chi-squared minimization.

The properties of the stellar wind and accretion stream are defined by free parameters, and therefore found through the minimization routine. The luminosity for Bondi-Hoyle accretion, as derived in chapter three, is dependant on three free parameters: the terminal wind velocity (v_∞), the companion star rotation speed parameter (f_1) and a normalization factor (κ). The luminosity from the gas stream is approximated as a density enhancement to Bondi-Hoyle accretion and is dependent on the same three free parameters plus four stream specific parameters: the density enhancement (d_s), the initial width (w_o), density periodicity (b) and the spreading speed (v_{sp}). For fixed mass and radius of the companion star, these seven free parameters are found for each system under the canonical assumption of the mass and radius of the neutron star being $R_n = 10\text{km}$ and $M_n = 1.4M_\odot$ respectively.

As shown in the subsequent sections of this chapter, the exact mass-radius relationship of the companions in the selected HMXBs is not well known. We can, however, put hard constraints on this relationship and then investigate an allowable range of masses and radii. The radius of the companion star in each chosen HMXB has an upper bound because they do not fill their Roche lobe. Due to the complexity of the Roche potential, a numerical approach (Eggleton 1983) is used to calculate the mean Roche lobe radius (R_{rl}) of the companion for each system.

$$\frac{R_{rl}}{a} = \frac{0.49q^{2/3}}{0.6q^{2/3} + \ln\left(1+q^{1/3}\right)} \qquad [5\text{-}2]$$

where q denotes the mass ratio $\frac{M_c}{M_n}$ of the system and a is the binary separation, given by

$$a = \left[P_{orb}^2 G \frac{M_c + M_n}{4\pi^2}\right]^{1/3} \qquad [5\text{-}3]$$

As discussed in chapter two, the mass of the companion star in each system is uniquely described by the system inclination (for fixed neutron star mass); thus inclination is used as a fixed parameter as a proxy for mass. The inclination of each system is constrained by the eclipse limit, and for systems without an observed eclipse (4U 1907+09, 2S 0114+650 and GX 301-2) the eclipse limit puts an upper bound on the system's inclination.

The following sections of this chapter will each be dedicated to one HMXB system and contain the same basic structure. A plot of mass versus radius displays the allowable region in mass-radius space in which the companion star can exist for each system. The fixed parameters, radius and inclination are chosen from this allowable range. Each section contains a table that displays the best fit free variables along with the associated minimum chi-squared value per set of fixed parameters of each system. Finally each section contains a plot of the best fit model compared to the observed light curve. The light curve created from the RXTE-ASM observations is plotted with open squares and the theoretical light curve for the wind and stream accretion model is shown with open circles. The wind and stream components of the model are displayed by a dotted line and dash-dot line respectively.

5.1 4U 1907+09

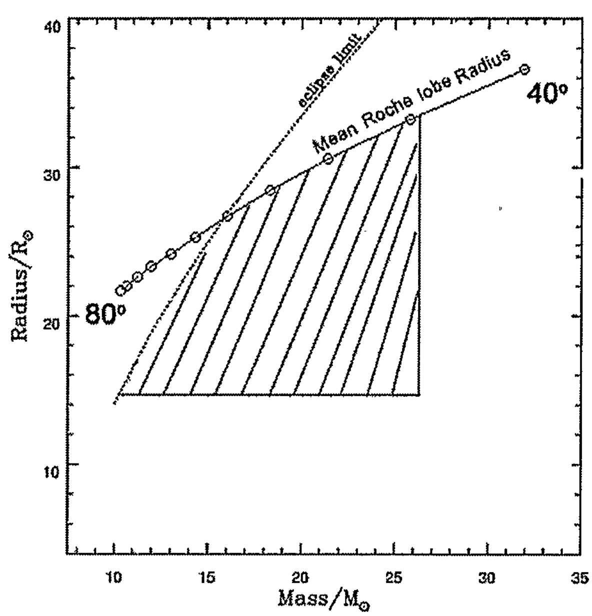

Figure 5-1 Radius vs. mass plot for the companion in 4U 1907+09. The Roche lobe limit (solid line with open circles) and eclipse limit (dotted line, from Roberts et al. 2001) are shown.

Optical spectroscopy is often used to help determine the mass and radius of the companion star in a HMXB (see Geis & Bolton 1986, Kaper et al. 1995, Reig et al. 1996). Strong reddening and faintness of the optical counterpart of 4U 1907+09 have hindered observations of its optical spectrum (Cox et al. 2005). In order to constrain the allowable values for mass and radius of the companion star in 4U 1907+09 other means were necessary.

Since its discovery there has been debate over the classification of the companion star in 4U 1907+09; van Kerkwijk et al. (1989) suggested the star was an OB supergiant, while Iye (1986) believed it to be a Be type star. Study of the interstellar atomic lines of Na I and K I present in the spectrum of the companion star indicated the distance to the system to be ~5kpc (Cox et al. 2005). This distance along with the strong reddening ($E_{B-V} = 3.45$) of the system proved incompatible with the classification of the companion as a Be type star (Cox et al. 2005). With the classification of the companion in 4U 1907+09 as an OB supergiant, further spectral analysis led to constraints on the inclination of the system. The large full width half max of the H-alpha line along with the observed projected rotational velocity of the companion star implied the system inclination should be ~55°-70° (Roberts et al. 2001). The inferred inclinations from Roberts et al. (2001) favour a smaller radius of the companion star, in order to keep the star from overflowing its Roche lobe (see Table 5.1). The absence of an observed eclipse in 4U 1907+09 puts a lower limit on the mass of the companion star (see Figure 5-1). These constraints define the allowable region in mass-radius space for the companion star which is shown by the thatched region of Figure 5-1.

Table 5.1 Mean Roche lobe radii for 4U 1907+09

Inclination	Mean Roche lobe radius
45°	32 $R_\odot$
50°	29 $R_\odot$
55°	27 $R_\odot$
60°	25 $R_\odot$
65°	24 $R_\odot$
70°	23 $R_\odot$

For 4U 1907+09 eccentricity along with the companion radius and system inclination, was investigated as a fixed parameter for the fitting routine. Table 5.2, Table 5.3 and Table 5.4 display best fit results using the radius and inclination as fixed parameters, for three different values of eccentricity: 0.25, 0.28, 0.31 respectively.

Table 5.2 Best fit values for 4U 1907+09 with eccentricity 0.25

R_c*	i*	v_∞ (km/s)	f_1	v_{sp} (km/s)	d_{s1}	w_o	κ (x 10^4)	b	χ^2
16 $R_\odot$	60°	989	0.99998	55	352	0.38 R_c	2.66	0.72	130
	65°	1092	0.99998	50	387	0.35 R_c	2.56	0.70	117
	70°	1149	0.99997	42	370	0.35 R_c	2.47	0.69	117
21 $R_\odot$	55°	2000	0.99998	90	10	0.13 R_c	523	0.50	155
	60°	2000	0.99998	42	158	0.28 R_c	21.9	0.41	92
	65°	2000	0.99998	46	142	0.25 R_c	15.3	0.26	112
26 $R_\odot$	45°	2000	0.99997	92	28	0.26 R_c	172	0	216
	50°	2000	0.99997	84	13	0.17 R_c	147	0	237
	55°	2000	0.99997	79	8	0.10 R_c	105	0	392

*Fixed Parameters

Table 5.3 Best fit values for 4U 1907+09 with eccentricity 0.28

R_c^*	i^*	v_∞ (km/s)	f_1	v_{sp} (km/s)	d_{s1}	K (x 10^4)	w_o	b	χ^2
16 $R_\odot$	60°	1424	0.99992	42	397	7.44	0.22 R_c	0.71	86
	65°	1550	0.99992	45	406	7.42	0.19 R_c	0.67	83
	70°	1547	0.99990	43	537	4.26	0.18 R_c	0.64	78
21 $R_\odot$	55°	1808	0.99998	79	79	34.3	0.17 R_c	0	102
	60°	2000	0.99998	61	42	55.7	0.15 R_c	0	100
	65°	2000	0.99998	56	20	69.8	0.12 R_c	0	108
26 $R_\odot$	45°	2000	0.99990	80	13	239	0.12 R_c	0.008	233
	50°	2000	0.99990	79	10	129	0.07 R_c	0.008	286
	55°	2000	0.99990	72	9	656	0.03 R_c	0.009	502

*Fixed Parameters

Table 5.4 Best fit values for 4U 1907+09 with eccentricity 0.31

R_c^*	i^*	v_∞ (km/s)	f_1	v_{sp} (km/s)	d_{s1}	K (x 10^4)	w_o	b	χ^2
16 $R_\odot$	60°	2000	0.99998	18	90	98.6	0.35 R_c	0.70	83
	65°	1801	0.99998	35	39	102	0.29 R_c	0.64	74
	70°	1842	0.99998	32	34	100	0.27 R_c	0.62	77
21 $R_\odot$	55°	1981	0.99998	63	15	165	0.22 R_c	0	92
	60°	2000	0.99998	59	10	153	0.16 R_c	0	101
	65°	2000	0.99998	62	9	111	0.13 R_c	0	159
26 $R_\odot$	45°	2000	0.99998	72	11	192	0.14 R_c	0	282
	50°	1746	0.99998	72	9	47.4	0.06 R_c	0	406
	55°	2000	0.99997	67	11	31.1	0.02 R_c	0	723

*Fixed Parameters

The results in Table 5.5 consider the radius of the companion star in 4U 1097+09 constant at 16.45 $R_\odot$ and then inclination and eccentricity are used as fixed parameters for the fitting routine.

Table 5.5 Best fit values for 4U 1907+09 with radius 16.45 $R_\odot$

e^*	i^*	v_∞ (km/s)	f_1	v_{sp} (km/s)	d_{s1}	κ (x 10^4)	w_o	b	χ^2
0.24	57°	1446	0.99992	56	795	6.50	0.26 R_c	0.74	105
	60°	1413	0.99992	59	772	4.85	0.24 R_c	0.72	105
	65°	1392	0.99992	58	483	5.20	0.22 R_c	0.69	103
0.26	57°	1468	0.99992	58	584	7.83	0.25 R_c	0.71	92
	60°	1483	0.99992	55	563	6.63	0.24 R_c	0.69	94
	65°	1393	0.99993	44	399	5.15	0.25 R_c	0.68	92
0.28	57°	1284	0.99990	47	431	5.14	0.30 R_c	0.69	88
	60°	1322	0.99989	42	301	6.36	0.29 R_c	0.67	88
	65°	1371	0.99988	44	480	3.30	0.25 R_c	0.64	86
0.30	57°	1410	0.99990	38	145	17.9	0.29 R_c	0.69	80
	60°	1514	0.99990	35	226	12.0	0.28 R_c	0.67	79
	65°	1462	0.89900	45	291	6.63	0.25 R_c	0.59	81
0.32	57°	1655	0.98800	38	38	105	0.25 R_c	0.66	74
	60°	1698	0.98700	37	28	123	0.23 R_c	0.63	69
	65°	1741	0.99281	40	17	150	0.20 R_c	0.59	72

*Fixed Parameters

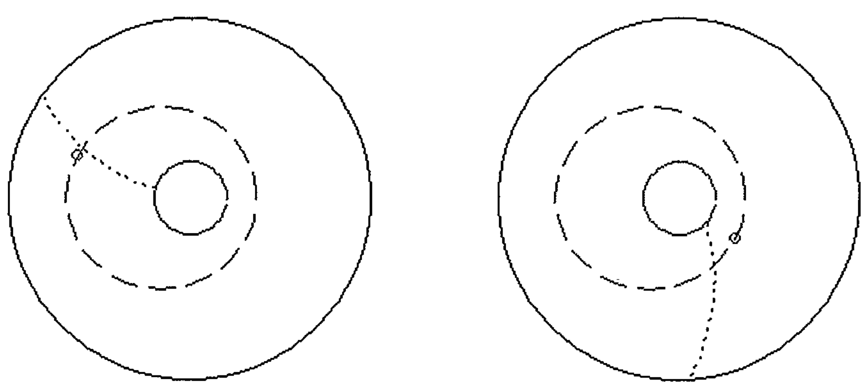

Figure 5-2 Geometry of 4U 1907+09 with e=0.31, R_c=16 $R_\odot$ and inc=65° (left: phase point 0.40, right: phase point 0.95). The central circle denotes the companion star and the accretion stream is represented by the dashed line. The neutron star (small circle) sits on its elliptical orbit (dashed line).

o

The theoretical light curve (solid line with circles) seen in Figure 5-3 contains two distinct peaks, a low broad peak near apastron and a sharp intense peak just before periastron. The apastron peak occurs as the stream catches up to but does not quite overtake the neutron star. The pre-periastron peak is a result of the neutron star travelling down the stream towards the companion star and the highest density portion of the stream (see Figure 5-2).

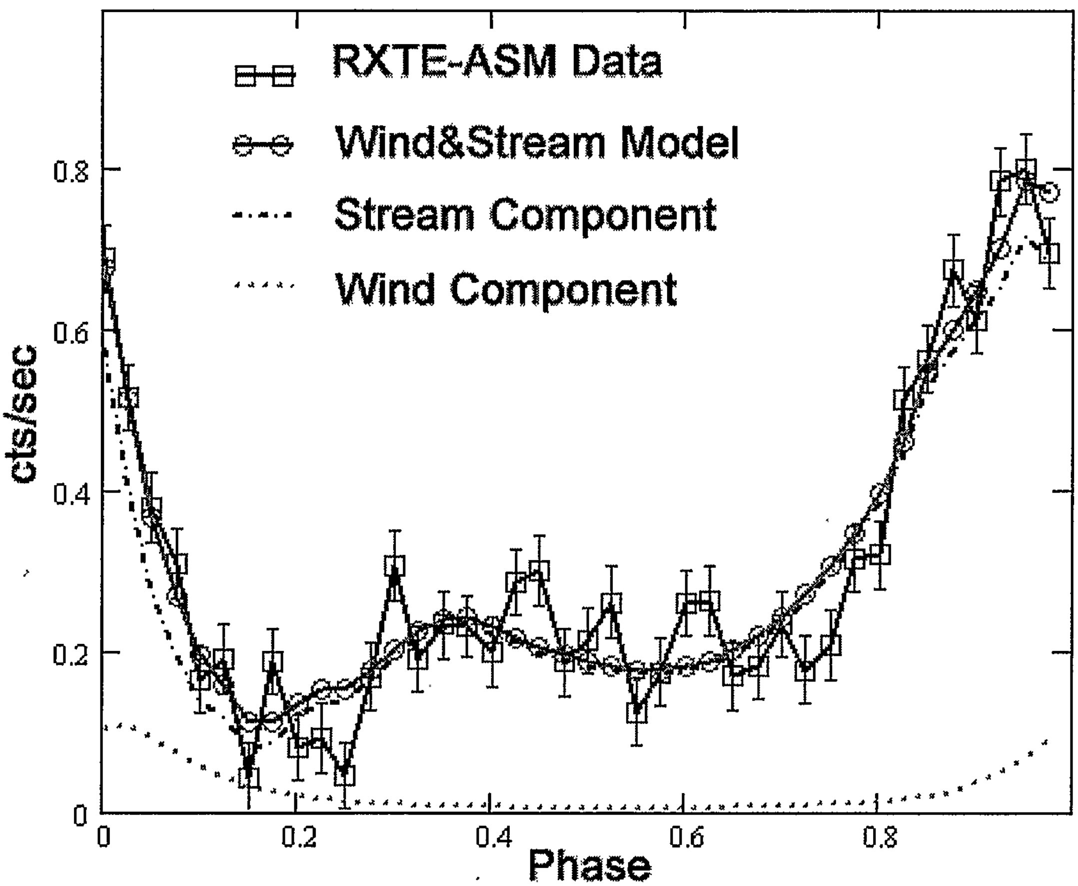

Figure 5-3 Model fit to RXTE-ASM light curve for 4U 1907+09 with e=0.31, R_c=16 $R_\odot$ and inc=65° (implies M_c=12.9 $M_\odot$).

5.1.1 Column Density Analysis

As a test of the stellar wind and accretion stream model of mass transfer in 4U 1907+09, I conducted a preliminary investigation of the column density of the system. Column density measures the amount of material along the line of sight to a stellar object and is typically measured in units of cm^{-2}. Fitting the observed orbital variation in column density for 4U 1907+09 with the theoretical column density from our stellar wind and accretion stream model serves as a check for the accretion luminosity model.

I constructed the column density as a function of orbital phase from RXTE-ASM observations. First the count rate simulator WebPIMMS, available online at NASA's High Energy Astrophysics Science Archive Research Center (HEASRC), was used to determine column density as a function of photon index and softness ratio of RXTE-ASM observations (see Figure 5-4). Observations of 4U 1907+09 have determined its photon index to be ~1.3 (Roberts et al. 2001). The softness ratio used in my thesis is the ratio of the 3-5 keV to 5-12 keV energy band observations from RXTE-ASM.

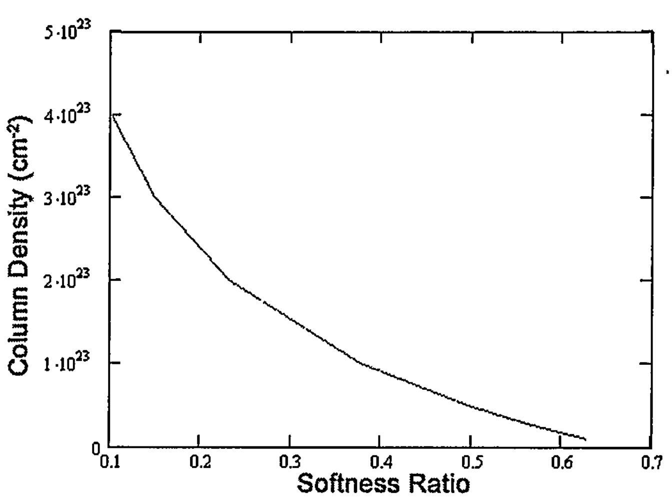

Figure 5-4 Column density versus RXTE-ASM softness ratio for photon index of 1.3, created using WebPIMMS.

The softness ratio as a function of orbital phase was constructed for 4U 1907+09 by dividing the 3-5 keV light curve by the 5-12 keV light curve (see Figure 5-5).

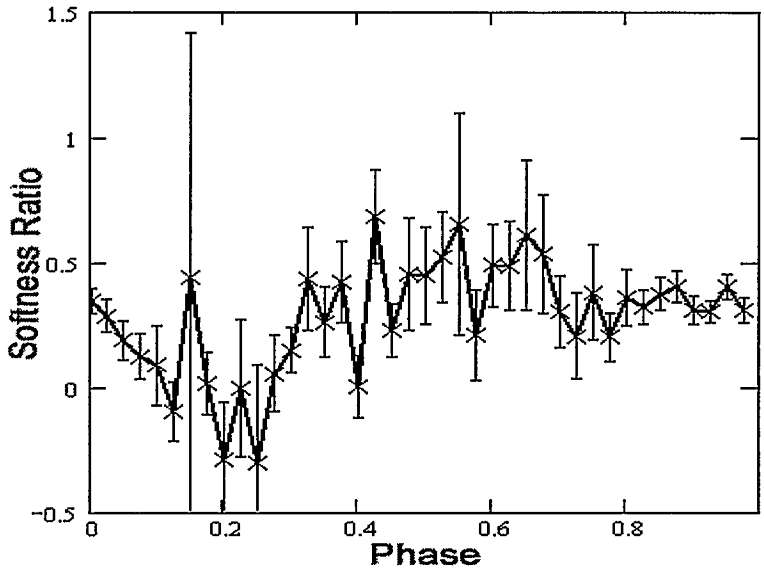

Figure 5-5 4U 1907+09 softness ratio.

Using the column density as a function of softness ratio and the softness ratio as a function of orbital phase, I derived the column density as a function of orbital phase for 4U 1097+09 (see Figure 5-6).

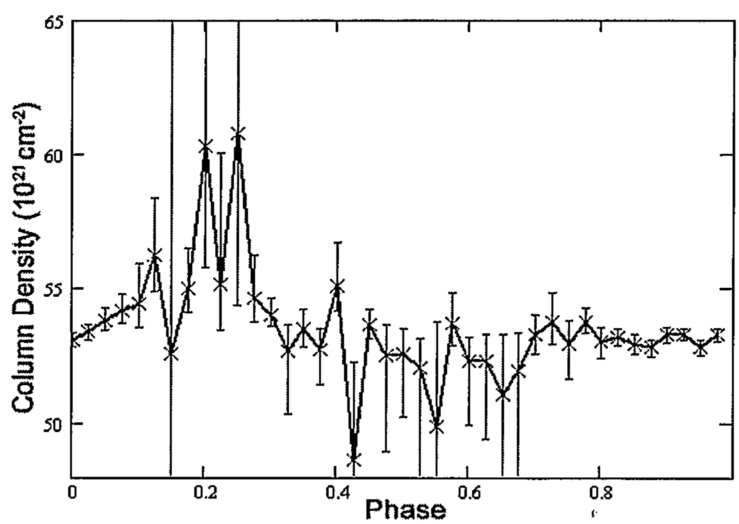

Figure 5-6 Column density as a function of orbital phase for 4U 1907+09.

The theoretical column density of an HMXB is found by integrating along the line of sight from infinity to the neutron star. The HMXB 4U 1907+09 is highly reddened by interstellar absorption (van Kerkwijk et al. 1989). For this analysis, the interstellar column density was taken to be $N_H^{is} = 4.8 \cdot 10^{22}\,\mathrm{cm}^{-2}$ which is comparable to the values used in other such analyses (van Kerkwijk et al. 1989, Roberts et al. 2001). The column density of the stellar wind and accretion stream model is approximated in my analysis as a summation along the line of sight from the neutron star to a distance of twice the binary separation.

The stellar wind is constantly blowing material radially outward from the companion star. Since the material is moving smoothly, the stellar wind is most dense near the companion star and the density drops off in the radial direction. Analytically the wind component of the column density is found as

$$N_H^{wind}(\dot{m}, v_\infty) = \dot{m}\int \frac{1}{4\pi r_{los}^2 v_{rad}(v_\infty, r_{los})} dr_{los} \qquad [5\text{-}4]$$

where $\dot{m}$ is the stellar mass loss rate of the companion star, r_{los} defines distance from the neutron star in the direction along the line of sight and v_{rad} is the radial wind velocity as described in chapter three (equation [3-28]).

The accretion stream contributes to the column density when it is positioned between the neutron star and the observer along the line of sight. In order to calculate the column density created by the stream first recall that the stream is modelled as a Gaussian density enhancement (D_{stream}) to the stellar wind.

$$D_{stream}(v_\infty, f_1, d_s, w_o, v_{sp}, b) = d_{s1}\left(d_s, v_\infty, b\right)\cdot \exp\left\{\frac{-\xi(f_1, v_\infty)^2}{2\sigma\left(w_o, v_{sp}, v_\infty\right)^2}\right\} \qquad [5\text{-}5]$$

To calculate the accretion luminosity from the stream, ξ was defined as the shortest distance from the center of the stream to the neutron star. In terms of column density, ξ is defined as the distance from the neutron star to the center of the stream along the line of sight. The stream component of the column density is found analytically as

$$N_H^{stream}(v_\infty, f_1, d_s, w_o, v_{sp}, b, \dot{m}) = \dot{m}\int \frac{1}{4\pi r_{los}^2 v_{rad}(v_\infty, r_{los})} d_{s1}\left(d_s, v_\infty, b\right)\cdot \exp\left\{\frac{-\xi_{los}(f_1, v_\infty)^2}{2\sigma\left(w_o, v_{sp}, v_\infty\right)^2}\right\} dr_{los}$$

[5-6]

Using the superposition of the summation approximations of equations [5-4] and [5-6] I was able to model the orbital variation to column density created by our stellar wind and accretion stream model. Figure 5-7 is a plot of the derived RXTE-ASM column density for 4U 1907+09 (solid line with crosses) with the wind and stream column density model (solid line with circles) as well as the wind (dotted line) and stream (dash-dot line) components to the column density model. The column density model is created for 4U 1907+09 with a companion radius of $R_c = 16R_\odot$, system inclination of $i = 60^o$, eccentricity of $e = 0.31$ and a value of $\dot{m} = 1.48\cdot 10^{-7} M_\odot \text{yr}^{-1}$ was used for the stellar mass loss rate. The remaining free parameters in the column density model were taken to be the best fit values from the accretion luminosity model for a companion radius of $R_c = 16R_\odot$, system inclination $i = 60^o$ and eccentricity $e = 0.31$.

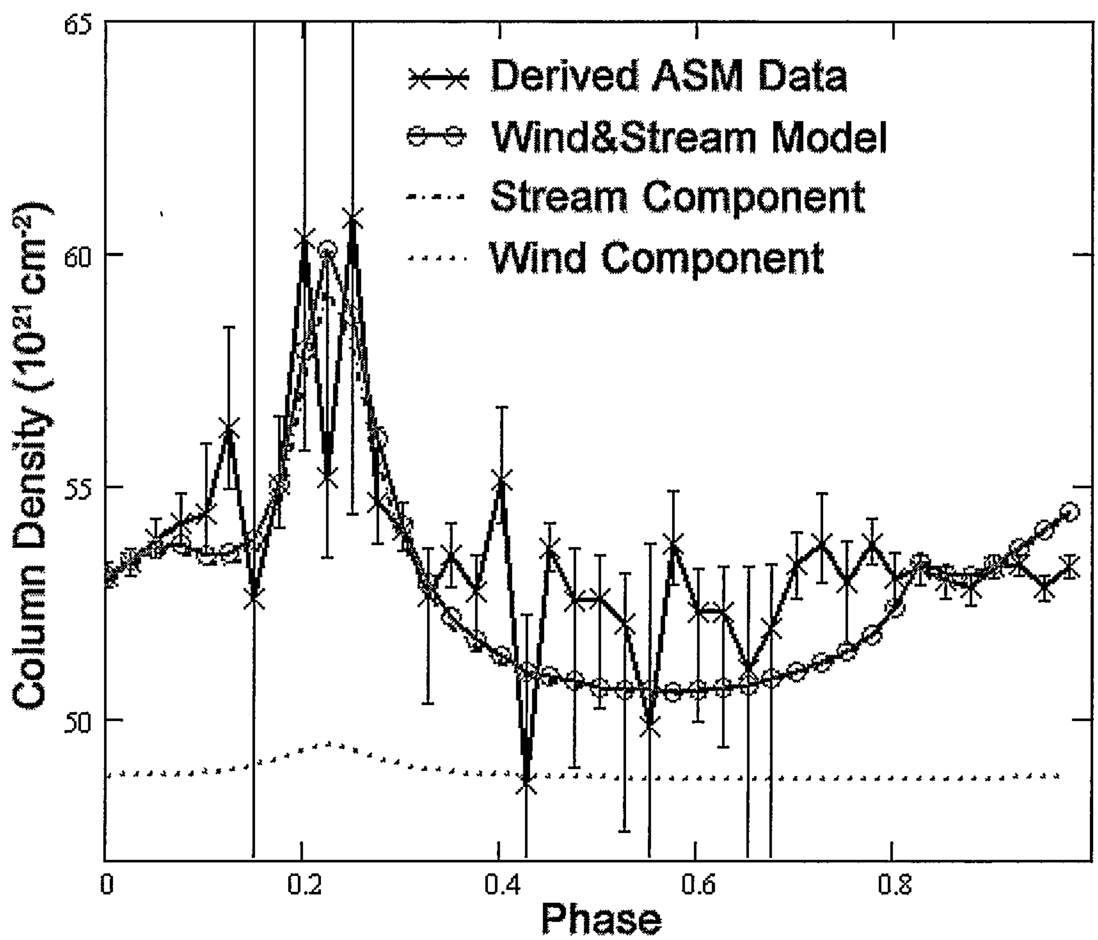

Figure 5-7 Column density model fits to RXTE-ASM derived data for 4U 1907+09. The column density model used the best fit parameters from the accretion luminosity model for 4U 1907+09 as inputs.

5.2 GX 301-2

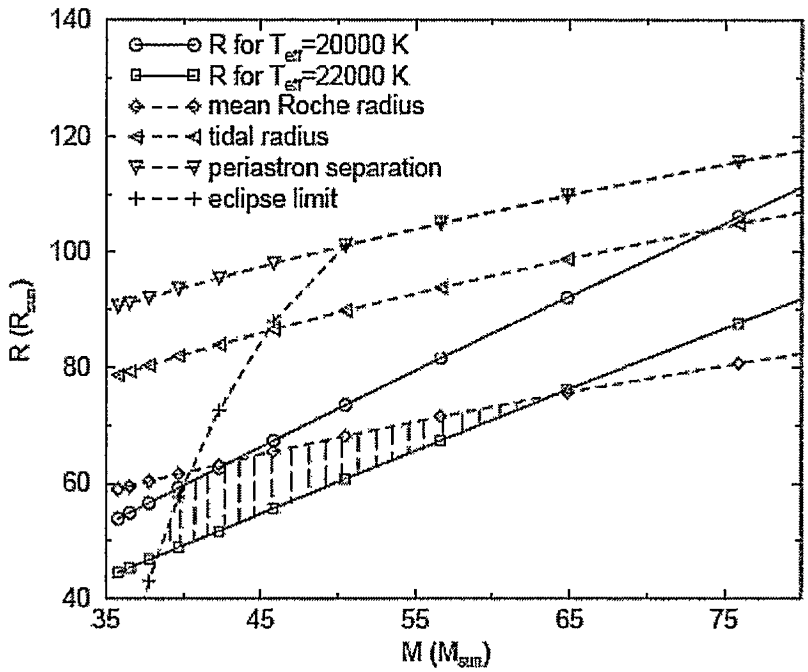

Figure 5-8 Radius vs. Mass plot for GX 301-2 (Leahy 2002).

GX 301-2 is one of the most well studied HMXB systems, thus there are strong constraints on the mass-radius relationship of the companion star as seen in Figure 5-8. The fixed parameters used in the fitting routine of this thesis were chosen from the thatched region of Figure 5-8. The left boundary of the thatched region comes from the fact that there is no observed eclipse for GX 301-2. The upper boundary of the thatched region is the constraint that the companion star in GX 301-2 has a smaller radius than its mean Roche lobe radius. The lower constraint for the thatched region of Figure 5-8 comes from optical observations. The spectral type of the companion star in GX301-2 is B2 Iae (Leahy 2002) and the effective temperature falls between 20000K and 22000K (Koh et al. 1997). The mass-luminosity relation of Koh et al. (1997), which comes from stellar models of Schaller et al. (1992) is used to plot the mass-radius relationships for T_{eff} = 20000K and T_{eff} = 22000K in Figure 5-8. The lower boundary of the thatched region comes from the T_{eff} = 22000K mass-radius curve.

The fitting routine was implemented for a selection of companion radius and system inclinations that fall within the thatched region of Figure 5-8. The best fit values for the free parameters of the model are displayed in Table 5.6.

Table 5.6 Best fit values for GX 301-2

R_c^*	i^*	v_∞ (km/s)	f_1	v_{sp} (km/s)	d_{s1}	w_o	κ (x 10^4)	b	χ^2
55 $R_\odot$	70°	732	0.51	76	87	0.19 R_c	669	0.71	1628
	73°	756	0.51	74	80	0.18 R_c	679	0.69	1650
	75°	710	0.54	72	73	0.17 R_c	514	0.67	1653
62 $R_\odot$	60°	633	0.38	63	65	0.17 R_c	474	0.66	1796
	65°	650	0.64	62	50	0.17 R_c	334	0.48	1864
	70°	647	0.65	87	39	0.02 R_c	271	0.03	1833
	75°	718	0.64	75	40	0.08 R_c	292	0	1945
68 $R_\odot$	60°	565	0.31	117	122	0.01 R_c	323	0.59	5001
	65°	259	0.63	71	17	0.01 R_c	34.6	0.10	4745
	70°	560	0.31	122	102	0.02 R_c	166	0.26	4908
75 $R_\odot$	55°	333	0.62	85	28	0.02 R_c	84.4	0.14	4085
	57°	599	0.32	131	151	0.01 R_c	291	0.41	4890
	60°	604	0.32	131	133	0.02 R_c	223	0.22	4902

*Fixed Parameters

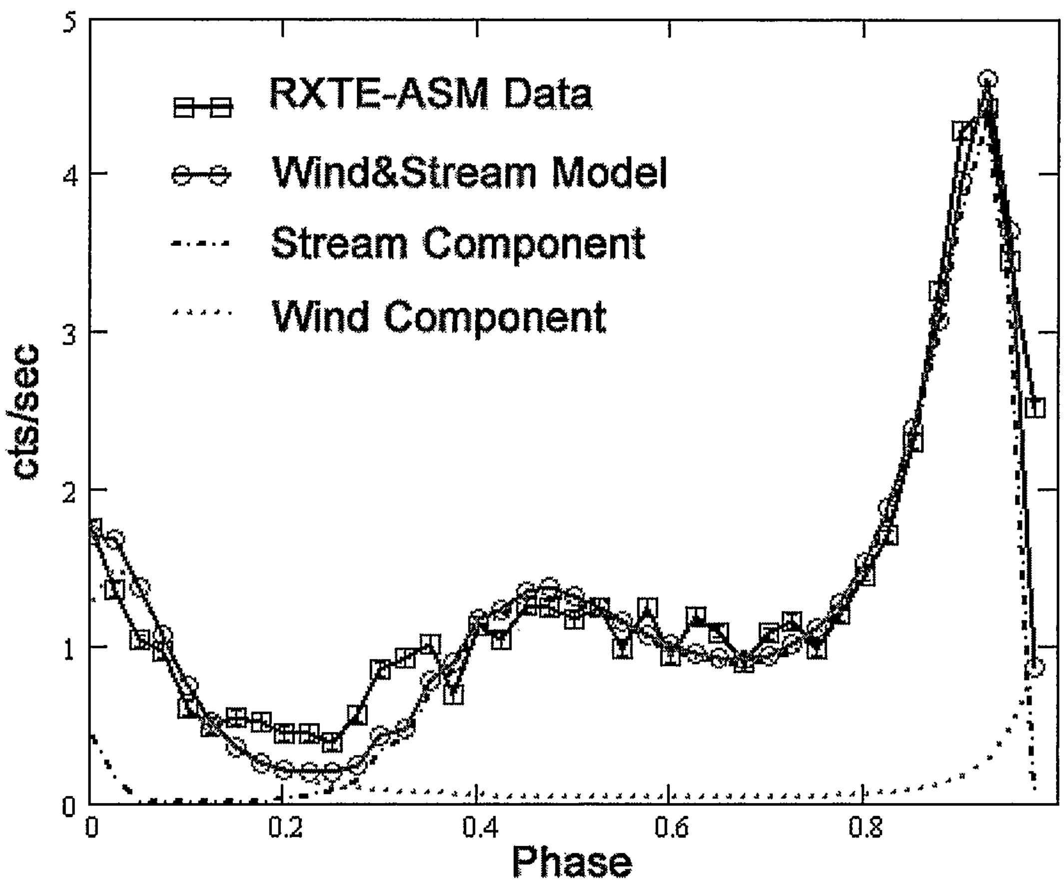

Figure 5-9 Model fit to RXTE-ASM light curve for GX 301-2 with R_c=62 $R_\odot$ and inc=60°(implies M_c=53.3 $M_\odot$).

The light curve for GX 301-2 (see Figure 5-9) displays the same double peak structure as 4U 1907+09. The high degree of eccentricity of GX 301-2 causes the neutron star to slow down enough at apastron such that the accretion stream overtakes the neutron star. As the neutron star accelerates towards periastron it once again passes through the accretion stream. See Figure 3-7 for a plot of the geometry of the system.

5.3 OAO 1657-415

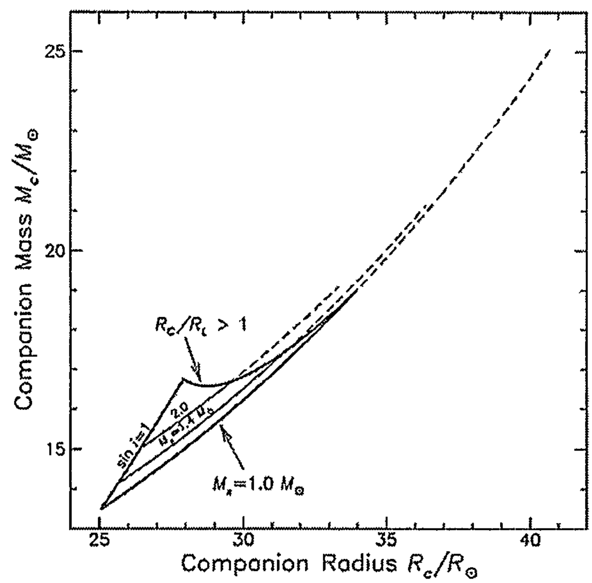

Figure 5-10 Mass vs. radius of the companion star in OAO 1657-415. From Chakrabarty 1993.

The mass and radius relationship of the companion star in OAO 1657-415 is constrained to exist within the region of Figure 5-10 bounded by the dark solid lines. The left boundary of the region is the simple constraint that the maximum allowable system inclination is, by definition, 90°. The upper boundary of the allowable region in Figure 5-10 describes the constraint that the companion star must have a smaller radius than its Roche lobe at periastron. The assumption that the mass of the neutron star is $1.4\,M_\odot$ is relaxed for the analysis of this system; instead a lower limit of $1\,M_\odot$ is used. The observed eclipse in OAO 1657-415 puts constraints on the radius of the companion (Chakrabarty et al. 1993). For chosen masses of the companion and primary star, the binary separation of the system can be determined (see equation [5-3]). Using the binary separation to describe the orbit of the neutron star along with the duration of the eclipse, the allowable radius of the companion star can be determined. The lower boundary to the allowable region in Figure 5-10 comes from the assumption that the neutron star must have a mass greater than 1 $M_\odot$.

Table 5.7 Best fit values for OAO 1657-415

R_c*	i*	v_∞ (km/s)	f_1	v_{sp} (km/s)	d_{s1}	κ	w_o	b	χ^2
25 $R_\odot$	80°	446	0.68600	109	3157	308	0.12 R_c	0	194
	85°	514	0.99995	115	3310	232	0.09 R_c	0	204
27 $R_\odot$	65°	442	0.99995	148	4505	247	0.10 R_c	0	198
	70°	444	0.99995	144	4149	188	0.08 R_c	0	179
	75°	439	0.99998	169	1826	293	0.04 R_c	0	233
	80°	440	0.99998	157	1674	269	0.04 R_c	0	204
29 $R_\odot$	67°	638	0.99995	137	5610	397	0.09 R_c	0	286
	70°	574	0.99995	146	4152	291	0.07 R_c	0	196
	72°	694	0.99995	131	5618	397	0.08 R_c	0	307
	75°	573	0.99995	146	3657	247	0.06 R_c	0	186
32 $R_\odot$	65°	692	0.99995	144	5092	359	0.05 R_c	0	542
	66°	732	0.99994	136	3307	627	0.05 R_c	0	558
	67°	725	0.99995	133	4684	397	0.05 R_c	0	537

*Fixed Parameters

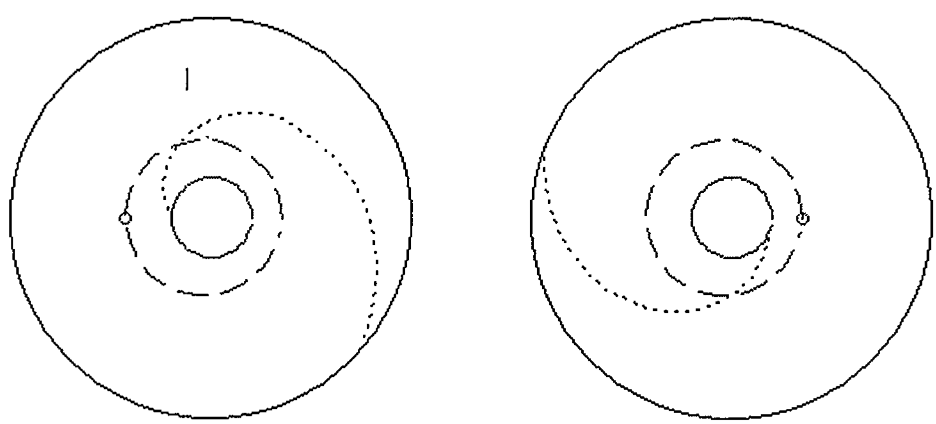

Figure 5-11 Geometry of OAO 1657-415 with Rc=27 $R_\odot$ and inc=70° (left: apastron, right: periastron). The central circle denotes the companion star and the accretion stream is represented by the dashed line. The neutron star (small circle) sits on its elliptical orbit (dashed line).

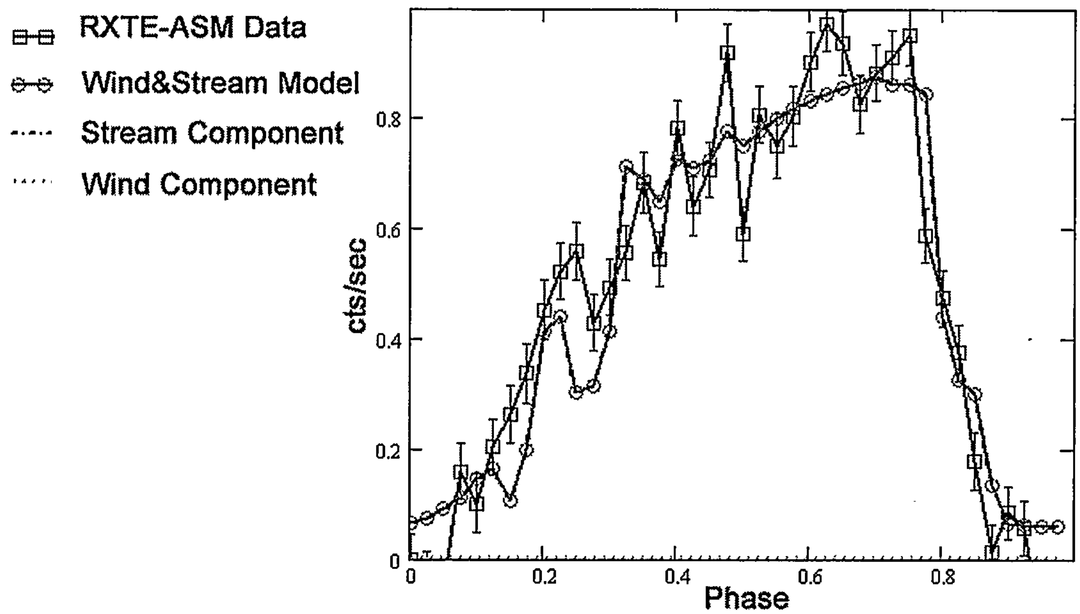

Figure 5-12 Model fit to RXTE-ASM light curve for OAO 1657-415 with R_c=27 $R_\odot$ and inc=70° (implies M_c=16.6 $M_\odot$).

The model plotted in Figure 5-12 as a fit to the RXTE-ASM orbital light curve displays jagged behaviour, especially around phase 0.2. This lack of smoothness in the model comes from the discreteness of the accretion stream approximation, which is most evident when calculating the closest approach point on the stream to the neutron star, as described in chapter three. The closest approach distance is found by comparing the distance from the neutron star to line segments of the stream defined by two consecutive stream points.

The overall shape of the theoretical light curve is almost entirely described by luminosity derived from the accretion stream. Unlike 4U 1907+09 and GX 301-2, the separation between the accretion stream and the neutron star in the HMXB OAO 1657-

415 does not change drastically over the orbit of the system; see Figure 5-11 for a diagram of the geometry of OAO 1657-415.

5.4 2S 0114+650

From optical spectroscopy, Reig et al. (1996) determined various astrophysical parameters of the system 2S 0114+650, including mass and radius ($M_c = 16 \pm 5 M_{\odot}$ and $R_c = 37 \pm 15 R_{\odot}$). The broad range of values for the companion radius in 2S 0114+650 is truncated by the fact that the maximum mean Roche lobe radius is ~42 $R_{\odot}$. For the statistical analysis of 2S 0114+650 the companion radius was chosen such that it was smaller than the mean Roche lobe for each inclination.

Table 5.8 Mean Roche lobe radii for 2S 0114+650

Inclination	Mean Roche lobe radii
35°	28 $R_{\odot}$
40°	31 $R_{\odot}$
45°	32 $R_{\odot}$
50°	34 $R_{\odot}$
55°	36 $R_{\odot}$
60°	38 $R_{\odot}$
65°	39 $R_{\odot}$
70°	40 $R_{\odot}$
75°	41 $R_{\odot}$
80°	41 $R_{\odot}$
85°	42 $R_{\odot}$

Table 5.9 Best fit parameters for 2S 0114+650

R_c*	i*	κ (x 10^4)	v_∞ (km/s)	f_1	χ^2
$25\,R_\odot$	35°	1.08	272	0	165
	40°	2.16	311	0	165
	45°	3.89	350	0	165
	50°	6.38	386	0	164
	55°	9.40	415	0	164
	60°	13.0	442	0	162
	65°	16.6	460	0	162
	70°	23.7	506	0	161
	75°	28.2	524	0	160
	80°	32.0	538	0	160
	85°	34.5	546	0	159
$30\,R_\odot$	45°	1.16	265	0	164
	50°	1.88	289	0	165
	55°	2.91	316	0	166
	60°	4.17	341	0	166
	65°	5.58	362	0	166
	70°	7.02	379	0	165
	75°	8.36	393	0	165
	80°	9.45	403	0	165
	85°	10.2	409	0	165
$38\,R_\odot$	65°	0.91	228	0	158
	70°	1.19	243	0	159
	75°	1.46	255	0	160
	80°	1.68	263	0	161
	85°	1.82	268	0	161

*Fixed Parameters

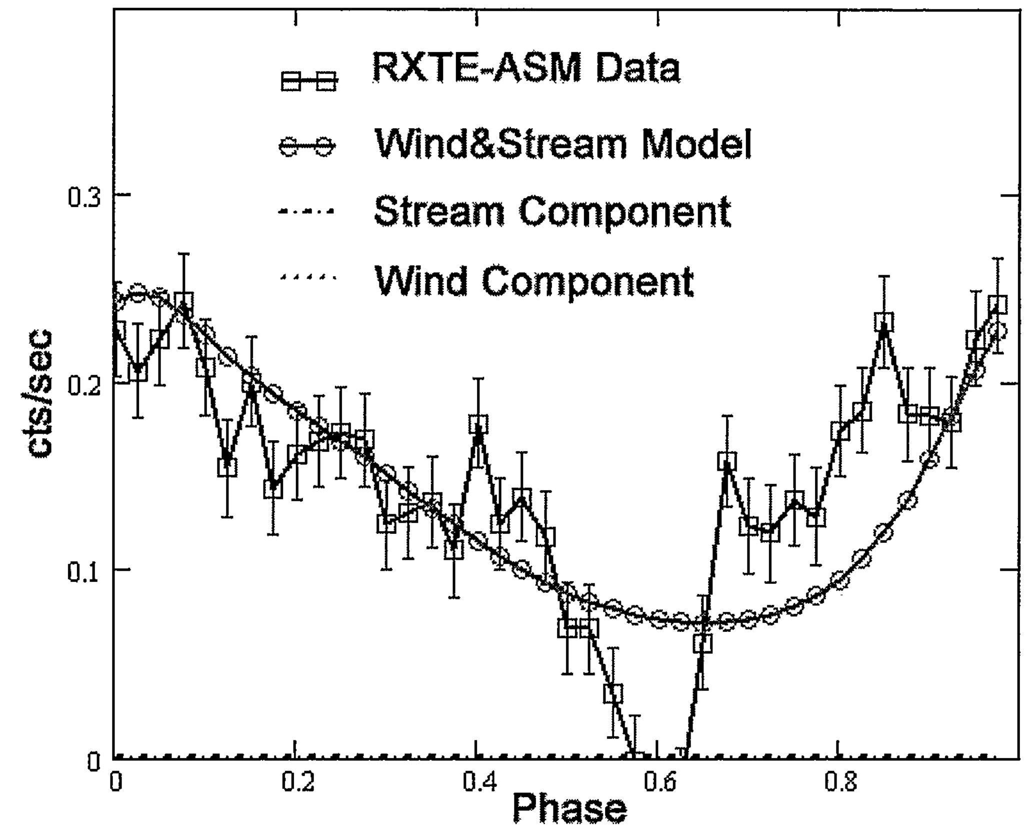

Figure 5-13 Model fit to RXTE-ASM light curve for 2S 0114+650 with R_c=38 $R_\odot$ and inc=65°.

Figure 5-13 shows the best fit of the model to the observed light curve of the system 2S 0114+650. The light curve is entirely described by luminosity from accretion of the stellar wind.

Chapter Six: Discussion

Many observed HMXBs that exhibit eccentric orbits present orbital variations in X-ray luminosity that cannot be described with stellar wind or disk accretion models (Friend & Castor 1982, Stevens 1988). In this research I consider accretion via strong stellar winds and a dynamic gas stream. This allows me to accurately model these orbital variations in X-ray flux. Through this research, I am able to determine properties of the stellar wind and accretion stream as well as global parameters of the companion star in each studied HMXB. This analysis was completed by fitting a wind and stream accretion model to observations. For each HMXB, the goodness of fit of the theoretical light curve to the light curve from the RXTE-ASM observations was measured using chi-squared analysis. The minimum chi-squared found for each system was large compared to the number of degrees of freedom (33 dof), thus statistically the model was not a good fit. The main contribution to the chi-squared for each system was fluctuations in the observations. The aberrations in the observed light curves are most likely caused by clumps in the stellar wind and gas stream (Leahy & Kostka 2008). The model used in my thesis considers smooth stellar wind and an accretion stream that is approximated as a uniform Gaussian density enhancement.

The discussion presented in this chapter will consider the fit of the overall shape of the model light curves to the observations, which was favourable for most systems.

6.1 4U 1907+09

The statistical fit of my wind and stream accretion model to the observed light curve for 4U 1907+09 was the best of all the HMXB systems studied in this thesis (reduced chi-squared of ~2). The overall shape of model light curve fit very well to the RXTE-ASM light curve. Both the sharp pre-periastron flare and low broad flare centered at about phase 0.4 were modelled by interactions of the neutron star with the accretion stream.

For each set of fixed parameters, the best fit results for the rotation speed of the companion star were values of ~100 km/s. This best fit value is in agreement with the rotational speed derived from spectroscopic study of the companion star in 4U 1907+09 (van Kerkwijk et al. 1989). The best fit terminal wind velocity found by the fitting routine was ~1600 km/s which is very close to the expected value for an O type Supergiant star (Cox et al. 2005). Actual measurements of the terminal wind velocity of 4U 1907+09 are hampered by the high interstellar extinction along the line of sight to the system (Cox et al. 2005). The spreading speed of the accretion stream serves as a reality check for the model. Physically there is no reason for the stream to spread at velocities much higher than the expected speed of sound in the gas (~25 km/s, from equation [3-23] with typical inputs for an O type Supergiant). The best fit result for the spreading of the stream typically was ~40 km/s, which is less than a factor of two greater than the predicted speed of sound in the gas.

I found that the accretion luminosity of 4U 1907+09 was best described by a companion star of radius ~16 $R_{\odot}$ and system inclination of 65°, which implies a companion mass of ~13 $M_{\odot}$. As well there was a trend of lower minimum chi-squared values for higher values of eccentricity; the best fit results were for an eccentricity of 0.32.

Further analysis of 4U 1097+09 was carried out by modelling the column density of the system. The observed column density was derived from RXTE-ASM observations of 4U 1907+09 using WebPIMMS. The derived column density may not be accurate because WebPIMMS does not account for electron scattering of the X-rays, only absorption. There is no easy way to model electron scattering, which can have the effect of either raising or lowering the observed column density. Fitting to the column density of 4U 1907+09 derived from absorption; our model used the best fit parameters from the accretion luminosity model as inputs and provided a good fit to the overall shape of the column density data. The shape of the theoretical column density curve is predominantly due to contribution from the accretion stream. The peak in column density at orbital phase ~0.2 occurs when the line of sight to the neutron star looks down the central axis of the stream (see Figure 6-1).

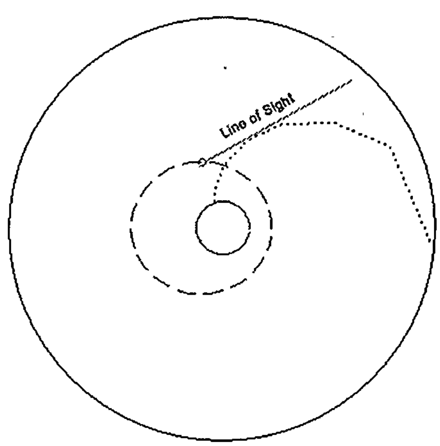

Figure 6-1 The HMXB 4U 1907+09 at orbital phase 0.2. The line of sight (solid line) points to the neutron star (small circle). The gas stream (dotted line) originates from the companion (central circle).

The column density model relies on one more parameter than the luminosity model, mass loss rate of the companion star. My best fit value for mass loss rate was $\dot{m} = 1.48 \cdot 10^{-7} M_{\odot} \mathrm{yr}^{-1}$. This stellar mass loss rate is lower than what was found by

Roberts et al. (2001), but is in good agreement with typical values for supergiant stars (Rosswog, 2007, p.227).

6.2 GX 301-2

The results of the statistical analysis for GX 301-2 show an increase in goodness of fit of my wind and stream accretion model to the RXTE-ASM observations for lower values of companion radius. The overall shape of the theoretical light curve fit well to the observed light curve for GX 301-2.

The typical best fit values of terminal wind velocity tend to fall between ~300km/s and ~700km/s which is in fair agreement with values derived from optical spectroscopy of the companion star (Kaper et al. 2006). The expression for rotational velocity of the companion in this model had a maximum value implying the star is rotating with the periastron angular velocity of the neutron star and a minimum value defined by the average orbital angular velocity of the neutron star. The best fit results of my wind and stream accretion model found the companion star to be rotating at an intermediate value, which would imply that the HMXB GX 301-2 is a young system. This is because torque on the companion from the primary star tends to increase the rotational velocity of the companion star over time (Carroll, 1996, p. 683). The best fit values of the spreading speed of the accretion stream were relatively high compared to the expected sound speed in the gas. This would imply that the constant spreading of the accretion stream is not a good model for the width of the stream. Perhaps hydrodynamic effects should be considered when describing the width of the accretion stream.

6.3 OAO 1657-415

The overall shape of the light curve for OAO 1657-415 is fit well by my stellar wind and accretion stream model, with the exception of irregularities caused by the approximations in the calculation of the accretion stream (discussed in section 5.3). The model that best fit the observations of OAO 1657-415 contains a tremendously dense accretion stream and limited contribution from stellar winds. The presence of a dense accretion stream without strong stellar winds is difficult to justify, thus in order to discuss the best fit model we must consider the observed light curve of OAO 1657-415 more closely.

The HMXB OAO 1657-415 contains an eclipsing orbit. The neutron star eclipse is centered nearly on periastron and lasts about 0.15 of the orbital phase (Chakrabarty et al. 1993). For an eccentric HMXB accreting material via stellar winds, there must be an increase in accretion at periastron due to the increased density of the wind (Bondi & Hoyle 1944). For OAO 1657-415 the neutron star is shielded along the line of sight by the companion around periastron and thus the observed light curve does not show the increase in accretion luminosity that is expected for that portion of orbital phase, if it is exhibiting mass transfer via stellar wind.

The stellar wind and accretion stream model used in my thesis does not consider the possibility of an eclipse. The fitting routine forces the model to suppress the wind component of the X-ray luminosity in order to account for the observed drop in luminosity around periastron caused by the eclipse in OAO 1657-415. The asymmetric shape of the observed light curve from phase points 0.1 to 0.9 of OAO 1657-415 is described well by the presence of a gas stream. The model was forced to suppress the wind component of accretion luminosity to accommodate the periastron eclipse. In order to compensate, the density enhancement factor of the stream was strengthened to reach the observed level of X-ray luminosity for OAO 1657-415.

The best fit results of my wind and stream accretion model to the light curve of OAO 1657-415 are encouraging, to date there is no consistent model for the method of accretion in this system (Barnstedt et al. 2008). Future work modelling OAO 1657-415 could be done with this stellar wind and accretion stream model with the inclusion of the effects of an eclipse added to the accretion algorithm. Using an eclipsing model, the overall shape of the light curve would still be described by the accretion stream; however the density enhancement factor would be reduced due to the increased presence of stellar wind accretion.

Study of the column density of OAO 1657-415 would help to understand the role of absorption in the X-ray luminosity of the system. I carried out preliminary research on the column density of OAO 1657-415 by investigating the softness ratio. The softness ratio of OAO 1657-415 was constructed from RXTE-ASM observations by dividing the 3-5 keV energy band light curve by the 5-12 keV energy band light curve.

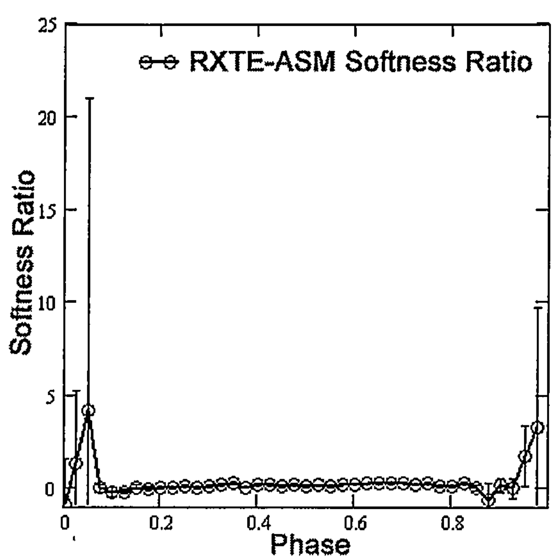

Figure 6-2 OAO 1657-415 Softness ratio

Unfortunately the RXTE-ASM data for OAO 1657-415 is too flat to extract a meaningful plot of column density from the softness ratio. Perhaps pointed observation from RXTE-PCA would shed light on the column density of OAO 1657-415 and its effect on the X-ray light curve.

6.4 2S 0114+650

The observed light curve of 2S 0114+650 was best fit by my accretion model when it only included stellar wind capture. These fitting results serve as a control experiment for the model. The wind and stream accretion model did not force the presence of a stream into the best fit results at any cost. Instead the fitting routine determined that stellar wind accretion alone is a more likely candidate for the accretion mechanism of this system, which agrees with other studies of 2S 0114+650 (Reig et al. 1996).

For each set of fixed parameters (companion radius and inclination) the best fit results of the wind model found that the companion star was slowly rotating, which is in agreement with observations of 2S 0114+650 (Farrell et al. 2008). The best fit results contained a trend towards lower values of terminal wind velocity with lower values of inclination for each fixed companion radius. As well a trend exists of increasing terminal wind velocity for decreasing values of companion radius at fixed values of inclination.

The overall shape of the model light curve is a reasonable fit to observations. A sharp dip exists in the observed light curve at approximately orbital phase 0.6, which may be due to an atmospheric eclipse of the neutron star (Farrell et al. 2008). As discussed in section 6.3, this accretion model does not describe the presence of an eclipse. The observed light curve of 2S 0114+650 contains a large degree of fluctuation which is most likely caused by clumps in the stellar wind.

6.5 Overview

Stevens (1988) made the suggestion that a correlation exists between eccentricity of the neutron star orbit and the presence of a gas stream in HMXBs. The most highly eccentric HMXB is GX 301-2 (see Table 2.2) and there is strong evidence, supported by my work in this thesis, that the system contains a gas stream (Haberl 1991, Leahy 1991, Leahy 2002, Leahy & Kostka 2008).

The analysis of 4U 1907+09 in my thesis reinforces this hypothesis. The HMXB contains a significantly eccentric orbit (see Table 2.2) and the X-ray light curve was fit very well by my wind and stream accretion model. The presence of a gas stream is further supported by preliminary analysis of the system's column density.

The possible existence of a gas stream in OAO 1657-415 implies that there are other factors that may lead to the creation of a gas stream in HMXBs, due to the low system eccentricity (see Table 2.2). However the eclipse in the light curve suggests that further analysis is required to support or refute the presence of a gas stream in OAO 1657-415.

6.6 Future Work

As determined by the analyses of 2S 0114+650 and OAO 1657-415, the ability to accurately model eclipses would benefit our accretion model. In order to model the light curve of an eclipsing binary, the phase of the eclipse would have to be identified and then only the non-eclipsing portion of the orbital phase would be used in the statistical analysis.

The width of the accretion stream in this model was described by the expansion of the gas at a constant rate (see equation [3-36]), giving the stream a conical shape in the inertial frame of the stream. Future versions of the stream accretion model should include variations on this shape, perhaps the presence of a shock front on the leading edge of the stream or varying the expansion rate as a function of radial distance from the companion star.

The preliminary study of the column density of 4U 1907+09 substantiated the claim that a gas stream was present in the system. Further analysis of the column density for all of the studied HMXBs would greatly help our understanding of the dynamics of the systems.

Bibliography

"High Energy Astrophysics Science Archive Research Center", http://heasarc.gsfc.nasa.gov/.

Barnstedt, J. et al. "INTEGRAL Observations of the Variability o fOAO 1657-415" Astronomy and Astrophysics 486.1 (2008): 293-302.

Baykal, A., Inam, S.C. and Beklen, E. "Evidence of a Change in Long-Term Spin-Down Rate of the X-ray Pulsar 4U 1907+09." Monthly Notices of the Royal Astronomical Society 369 (2006): 1760-1764.

Bildsten, L. et al. "Observations of Accreting Pulsars." Astrophysical Journal Supplement Series 113 (1997): 367-408.

Bondi, H. and Hoyle, F. "On the Mechanism of Accretion by Stars." Monthly Notices of the Royal Astronomical Society 104 (1944): 273-282.

Carroll, B.W. and Ostlie, D.A. An Introduction to Modern Astrophysics. Reading: Addison-Wesley, 1996.

Castor, J.I., Abbott, D.C. and Klein, R.I. "Radiation-Driven Winds in Of Stars." Astrophysical Journal 195 (1975):157-174.

Chakrabarty, D. et al. "Discovery of the Orbit of the X-ray Pulsar OAO 1657-415." Astrophysical Journal 403 (1993): L33-L37.

Cox, N.L.J., Kaper, L. and Mokiem, M.R. "VLT/UVES Spectroscopy of the O Supergiant Companion to 4U 1907+09(7)." Astronomy and Astrophysics 436 (2005): 661-669.

Edgar, R. "A Review of Bondi-Hoyle-Lyttleton Accretion." New Astronomy Reviews 48.10 (2004): 843-859.

Eggleton, P.P. "Approximation to the Radii of Roche Lobes." Astrophysical Journal 268 (1983):368-369.

Endo, T. "Probing Circumstellar Matter with X-ray Binary Pulsars" Ph.D. thesis, University of Tokyo, 2000.

Farrell, S.A. et al. "A Detailed Study of 2S 0114+650 with the Rossi X-ray Timing Explorer." Monthly Notices of the Royal Astronomical Society 389 (2008): 608-628.

Forman, W. et al. "The Fourth Uhuru Catalog of X-ray Sources." Astrophysical Journal Supp. 38 (1978): 357-412.

Frank, J., King, A. and Raine, D. Accretion Power in Astrophysics Third Edition. Cambridge: Cambridge UP, 2002.

Friend, D.B. and Castor, J.I. "Radiation-Driven Winds in X-ray Binaries." Astrophysical Journal 261 (1982): 293-300.

Gies, D.R. and Bolton, C.T. "The Optical Spectrum of HDE 226868 = Cygnus X-1. III. A Focused Stellar Wind Model for He II lambda 4686 Emission." Astrophysical Journal 304 (1986): 389.

Goldstein, H., Poole, C. and Safko, J. Classical Mechanics Third Edition. San Francisco: Addison Wesley, 2002.

Grundstrom, E.D. et al. "Joint H-alpha and X-ray Observations of Massive X-ray Binaries. I. the B Supergiant System LS I +65 010 = 2S 0114+650." Astrophysical Journal 656 (2007): 431-436.

Haberl, F. "The X-ray Properties of GX 301-2 (4U 1223-62)." Astrophysical Journal 376 (1991): 245-255.

Hewish, A. et al. "Observation of a Rapidly Pulsating Radio Source." Nature 217 (1968): 709-713.

Iben, I. "Stellar Evolution: Comparison of Theory with Observations." Science 155.3764 (1967): 785-796.

Iye, M. "High-Resolution Spectrum of the Peculiar Optical Counterpart of the X-Ray Binary Pulsar 4U 1907+09." Publication of the Astronomical Society of Japan 38 (1986): 463-473.

Jahoda, K. et al. "In-Orbit Performance and Calibration of the Rossi X-ray Timing Explorer (RXTE) Proportional Counter Array (PCA)." SPIE 2808 (1996): 59-70.

Kaper, L. et al. "VLT/UVES Spectroscopy of Wray 977, the Hypergiant Companion to the X-ray Pulsar GX301-2." Astronomy and Astrophysics 457.2 (2006): 595-610.

Kaper, L. et al. "Wray 977 (GX301-2): A hypergiant with Pulsar Companion." Astronomy and Astrophysics 300 (1995): 446-452.

Koh, D.T. et al. "Rapid Spin-Up Episodes in the Wind-Fed Accreting Pulsar GX 301-2." Astrophysical Journal 479 (1997): 933-947.

Lajoie, C.P. and Sills, A. "Mass Transfer in Binary Systems: A Numerical Approach." Dynamical Evolution of Dense Stellar Systems, Proceedings of the International Astronomical Union, IAU Symposium 246 (2008): 271-272.

Lattimer, J. M. et al. "The Physics of Neutron Stars." Science 304 (2004): 536-542.

Leahy, D.A. "Evidence for a Gas Stream in GX301-2." Monthly Notices of the Royal Astronomical Society 250 (1991): 310-313.

Leahy, D.A. "Mapping the Shape of the Accretion Disk of Hercules X-1." Astronomische Nachrichten 325 (2004):205-208.

Leahy, D.A. "The RXTE/ASM X-ray Light Curve of GX301-2." Astronomy and Astrophysics 391 (2002): 219-224.

Leahy, D.A. and Kostka, M. "Stellar Wind Accretion in GX 301-2: Evidence for a High-Density Stream." Monthly Notices of the Royal Astronomical Society 384 (2008): 747-754.

Levine, A. et al. "First Results from the All-Sky Monitor on the Rossi X-ray Timing Explorer." Astrophysical Journal 469 (1996): L33-L36.

Mukherjee, U. and Paul, B. "Orbital Phase Spectroscopy of GX 301-2 with RXTE-PCA." Astronomy and Astrophysics 427 (2004): 567-573.

Oppenheimer, J. R. and Volkoff, G. M. "On Massive Neutron Cores." Physical Review 55 (1939): 374-381.

Owen, M.P. and Blondin, J.M. "3-D Hydrodynamic Simulation of Accretion Disk Formation in LMC-X4." Accretion Phenomena and Related Outflows; IAU Colloquium 163. ASP Conference Series 121 (1997): 779.

Prakash, M. J. "Quark Matter and the Astrophysics of Neutron Stars." Journal of Physics G: Nuclear and Particle Physics 34.8 (2007): S253-S260.

Regos, E., Bailey, V.C. and Mardling, R. "Mass Transfer in Eccentric Binary Stars." Monthly Notices of the Royal Astronomical Society 358 (2005): 544-550.

Reig, P. et al. "Astrophysical Parameters of the Massive X-ray Binary 2S 0114+650." Astronomy and Astrophysics 311 (1996): 879-888.

Rhoades, C.E. and Ruffini, R. "Maximum Mass of a Neutron Star." Physical Review Letters 32.6 (1974): 324-327.

Roberts, M. et al. "Phase-Dependent Spectral Variability in 4U 1907+09." Astrophysical Journal 555 (2001): 967-977.

Rosswog, S. and Bruggen, M. Intronduction to High-Energy Astrophysics. Cambridge: Cambridge UP, 2007.

Schaller, G., Schaerer, D. and Maeder, G. "New Grids of Stellar Models from 0.8 to 120 solar masses at Z=0.02 and Z=0.001." Astronomy and Astrophysics 96 (1992): 269-331.

Skinner et al. "Discovery of 69 MS Periodic X-ray Pulsations in A0538-66." Nature 297 (1982): 568-570.

Stella, L., White, N.E. and Rosner, R. "Intermittent Stellar Wind Accretion and the Long-Term Activity of Population I Binary Systems Containing an X-ray Pulsar." Astrophysical Journal 308. (1986): 669-679.

Stevens, I.R. "An Enhanced Stellar Wind Accretion Model for Binary X-ray Transients." Monthly Notices of the Royal Astronomical Society 232 (1988): 199-213.

Thorsett, S.E. and Chakrabarty, D. "Neutron Star Mass Measurements. I. Radio Pulsars." Astrophysical Journal 512 (1999): 288-299.

van Kerkwijk, M.H., van Oijen, J.G.J. and van den Heuvel, E.P.J. "Extended Optical Spectroscopy of the Massive Companion of 4U 1907+09." Astronomy and Astrophysics 209 (1989): 173-182.